Spinning disk atomization

Shikhmurzaev, Yulii; Sisoev, Grigory; Li, Yuan

DOI:
10.1063/1.5044429

Document Version
Publisher's PDF, also known as Version of record

Citation for published version (Harvard):
Shikhmurzaev, Y, Sisoev, G & Li, Y 2018, 'Spinning disk atomization: theory of the ligament regime', *Physics of Fluids*, vol. 30, 092101. https://doi.org/10.1063/1.5044429

Spinning disk atomization: Theory of the ligament regime

Yuan Li, Grigori M. Sisoev, and Yulii D. Shikhmurzaev

Citation: Physics of Fluids **30**, 092101 (2018); doi: 10.1063/1.5044429
View online: https://doi.org/10.1063/1.5044429
View Table of Contents: http://aip.scitation.org/toc/phf/30/9
Published by the American Institute of Physics

Spinning disk atomization: Theory of the ligament regime

Yuan Li,[1] Grigori M. Sisoev,[2] and Yulii D. Shikhmurzaev[1,a)]
[1]*School of Mathematics, University of Birmingham, Birmingham B15 2TT, United Kingdom*
[2]*Institute of Mechanics, Lomonosov Moscow State University, Moscow 119192, Russia*

(Received 12 June 2018; accepted 20 August 2018; published online 12 September 2018)

A method of the mathematical modeling of the spinning disk atomization process as a whole, from the film flow on a rotating disk to the drop formation and detachment from the ends of the ligaments spiralling out of the disk's rim, is formulated and the key results illustrating its implementation are described. Being one of the most efficient nozzle-free atomization techniques, spinning disk atomization is used in many applications, ranging from metallurgy to pharmaceutical industry, but until now its design and optimization remain empirical which is time consuming and costly. In the present work, the entire spinning disk atomization process is, for the first time, modelled mathematically by (a) utilizing all known analytic results regarding its elements, notably the film flow on the disk and the dynamics of outgoing spiral jets, where the flow description can be simplified asymptotically and (b) using the full-scale numerical simulation of the three-dimensional unsteady free-boundary flow in the transition zone near the disk's rim which brings these elements together. The results illustrating the developed modeling approach reveal some previously unreported qualitative features of the spinning disk atomization process, such as the drift of the outgoing ligaments with respect to the disk, and elucidate the influence of physical factors on the size distribution of the drops and, where this is the case, satellite droplets. The comparison of the obtained results with available experimental data confirms the validity of the assumptions used in the modeling. *Published by AIP Publishing.*
https://doi.org/10.1063/1.5044429

I. INTRODUCTION

In many applications, it becomes necessary to "atomize" a body of liquid, disintegrate it into tiny and preferably uniform droplets, by manipulating the action of capillary forces that create them.[1,2] One of the most efficient and cheap ways of doing this is via the process known as spinning disk atomization (SDA).[1,3–6] The essence of the process is that a continuous stream of fluid is fed onto the central area of a horizontally orientated disk spinning about its vertical axis so that the centrifugal force drives the fluid away from the axis of rotation ensuring a continuous film flow over the disk's surface, and as the fluid reaches the disk's rim, it leaves the disk and breaks into drops. This happens in one of the following ways, depending on the flow parameters.[3,5,6] In the "direct droplet mode," which corresponds to low flow rates of the fluid supply, the film as such stays on the disk and the centrifugal force makes the drops break away straight from the film at the disk's rim. At higher flow rates, one has the "full ligament mode," where, on reaching the disk's rim, the film breaks into a number of jets ("ligaments") which spiral away from the disk, and as the capillary instability in these jets develops, they disintegrate into drops. Finally, at high flow rates, the process of atomization occurs in the "sheet mode," where the film flowing over the disk leaves it as a free liquid sheet which then breaks into ligaments and these into separate drops. To give an idea of the typical numbers involved, we can cite an experimental work by Peng *et al.*[5] showing that, for a 60% glycerol-water solution and the disk of radius 2.5 cm rotating at the angular velocity of 157 rad/s, the direct droplet mode, the fully developed ligament mode, and the free sheet mode correspond to the flow rates of 0.8, 3.2, and 16.4 ml/s, respectively. In Ref. 5, one can also find empirical correlations proposed by different authors for the critical regimes where one mode of atomization turns into another. It should be noted though that additional physical factors, like the gaseous crossflow,[7,8] can potentially affect the atomization results and, possibly, even the regime boundaries.

Technologically, each of these basic scenarios has its own issues, advantages, and disadvantages with regard to technological objectives and controllability of the process. In this study, we are interested in the full ligament regime, or in fact a class of regimes, where drops are produced from the jets that spiral out from the disk's rim.[3] As experiments show,[9] the full ligament mode ensures a narrower range of drop sizes than the sheet mode, whilst compared with the direct drop mode, it not only has higher productivity/flow rate but also, as an analysis of the dripping-jetting transition suggests,[10] can produce finer drops. These features make the full ligament regime attractive for many applications, including, for instance, powder manufacturing in metallurgy[11] and various chemical[12] and biomedical[13] technologies.

Although, as reviewed in Refs. 6, 14, and 15, quite a few empirical formulas have been proposed over the years to correlate the outcome of the SDA process with its control parameters and properties of the fluids, it is only a theoretical description accounting, in a coherent methodologically

a)Author to whom correspondence should be addressed: y.d.shikhmurzaev@bham.ac.uk

justifiable way, for the physical factors involved and their interaction that would allow one to optimize known SDA technologies and extend them to the regimes and fluids beyond the empirically investigated range.

From the modeling viewpoint, the SDA process in the ligament regime combines several flow elements: (a) the film flow over a spinning disk, (b) a three-dimensional and, in general, unsteady free-boundary flow in the transition zone, i.e., the region near the disk's rim, where the film splits into jets, (c) the dynamics of a curved capillary liquid jet that spirals away from the disk, including the propagation of disturbances along it, and, finally, (d) the dynamics of the capillary breakup leading to the formation of drops at the jet's end. Although some elements of the SDA process, notably the film flow over a spinning disk and the disintegration of jets into drops, have been the subject of intensive research, a theoretical description of the SDA process as a whole, which would incorporate what is known about the process elements and link them together via accurate simulation of the three-dimensional unsteady free-boundary flow in the transition zone, is still lacking. At the same time, the complexity of the SDA process calls for its theoretical description since an attempt to find the optimal parameters for a preset technological objective via experimental trial-and-error, besides being time-consuming and costly, would require finding a window, often narrow, in the parameter space by manipulating the control parameters none of which has a direct and obvious influence on the outcome. It should be noted also that small variations of the physical properties of the fluid, i.e., density, viscosity, and the surface tension, can affect the development of the velocity profile and thus the overall atomization process.[16] On the other hand, a head-on numerical simulation of the entire SDA process with the accuracy, especially in tracking the free surface, required for the outcome to be of practical use is well beyond what can be achieved even in the foreseeable future as it would involve computing a three-dimensional unsteady free-boundary flow on vastly disparate length and time scales.

In order to make the problem tractable, one has to utilize all known analytic simplifications regarding particular elements of the SDA process, thus facilitating their numerical simulation, simulate the missing elements where no analytic simplification is possible, and, most importantly, develop a method of matching all elements of the flow in a way that ensures the exchange of essential information between them and hence the integrity of the modeling of the SDA process as a whole.

In this paper, we present a theory of SDA in the ligament regime modeling the process in its entirety by implementing the approach outlined above, the main results it produces regarding particular features of the process that are difficult to investigate experimentally, and a comparison of the theoretical prediction of the drop sizes with available experiments. The paper is organized as follows. In Sec. II, we give an outline of the main results obtained for the key elements that form the SDA flow. Section III describes the problem formulation and the simplifications that can be made in the film and the jet regions. This section brings in what is known in these areas and introduces the unified scales to be used for the problem as a whole. Section IV outlines the computational scheme used to simulate the flow in the transition zone between the film and the jet regions and the matching conditions needed to match the flows in all three domains. In Sec. V, we consider the generation of disturbances in the outgoing jets which leads to the formation of drops. Section VI describes the simulation results for the waveless and the wavy film flows on the disk and the comparison of the former with available experiments. In Sec. VII, we summarize the main points of the paper.

II. BACKGROUND

The most well-studied element of those that form the SDA process is the film flow over a spinning disk, which is used, besides the SDA and encapsulation technologies,[17] also for the reaction intensification in polymer[18] and pharmaceutical industries[19,20] as well as for spin coating,[21] including two-layer coating.[22,23]

Schematically, the main findings regarding this flow can be summarized by considering the film flow over a disk of a very large (infinite) radius. Then, with the edge effects removed from consideration, one can observe a succession of different flow regimes characterized by their wave patterns, as reviewed in Ref. 24. For a given fluid, the regimes depend on (a) the flow rate, (b) the speed of rotation, and (c) the distance from the axis of rotation.[25–27]

Broadly, at low flow rates, the film driven away from the axis of rotation by the centrifugal force, being waveless in the vicinity of the axis, further afield develops an instability resulting in an axisymmetric wave pattern and further away from the disk's axis, an instability in the azimuthal direction kicks in so that the film disintegrates into a number of rivulets and the latter into drops. At higher flow rates, before the disintegration of the film into rivulets takes place, one can observe spiral waves superimposed on the axisymmetric ones.[25,26] Furthermore, as pointed out in a targeted study,[28] at sufficiently high flow rates and speeds of rotation, one can observe no less than four different wave regimes. First, in the inlet region close to the axis of rotation, there is (i) a smooth waveless flow which, as the instability develops, further afield, turns into (ii) a laminar-wave regime with axisymmetric waves. Then, at a greater distance from the axis, the laminar-wave regime turns into (iii) a "turbulent" regime characterized by disordered ripples on the free surface, which further afield degenerates into (iv) the second laminar-wave regime as the amplitude of the "turbulent" ripples is damped by viscosity as the mean thickness of the film decreases. Then, further away from the axis of rotation, one has the same scenario as in the case of low flow rates. It is necessary to clarify here that, in the present context, the term "turbulent" refers only to the chaotic character of waves appearing on the free surface of the film and not to the bulk flow. The latter remains laminar.

Depending on the flow rate and the speed of rotation, one can also observe irregular wave patterns.[29] It should be noted also that, as pointed out in Ref. 24, there is some discrepancy in experimental evidence rooted, apparently, in the complexity of measurements.

This remarkable richness of possible scenarios is complicated even further by the fact that for the same flow conditions one can observe a variety of different waves. This aspect of

the problem is best illustrated by looking at the film flow down an inclined plane, in particular, at the so-called "falling film flow," where the plane is vertical, which shares its most essential features with the film flow over a spinning disk but, unlike the latter, makes them easier to observe. In this flow, gravity takes the role of the centrifugal force in driving the film and the development of the wave pattern is much slower and spatially more extended than in the spinning disk one. The seminal paper by Kapitza and Kapitza[30] and many experiments performed in its wake[31] show that, generally, in the falling film flow, the same flow conditions for the same fluid produce different waves, i.e., an irregular wave pattern. However, the imposition of an external frequency at the inlet of the film synchronizes the waves and creates a reproducible periodic wave pattern which, as the frequency is reduced, transforms into the solitary-type waves ("pulses"). A similar behavior was observed in film flows down an inclined plane,[32–34] where the externally imposed frequency also synchronized the waves. Far away from the inlet, where the effect of the inlet conditions attenuates, the waves gradually lose their stability and further down this results in a chaotic flow regime. Experiments on the film flow over a spinning disk[27] analyzed in Ref. 35 show that the measured waves are the ones theoretically described as the so-called "dominating waves" and their characteristics are determined by their frequencies.

In the SDA process, the disk's edge can come into play in any of the aforementioned flow regimes, depending on the fluid, the disk size and parameters of the process, and hence the subsequent free-surface flow in the transition zone between the film and the outgoing jets and the dynamics of the jets leaving the disk can be generated by very different disk flow scenarios.

The dynamics of spiralling and, more generally, curved liquid jets involves two elements of difficulty compared with much studied dynamics of uniform straight jets. First, to make use of the disparate length scales along and across the jet in the slender-jet approximation, one has to introduce a jet-specific and, in general, non-orthogonal coordinate system[36] and describe the flow using it. As reviewed in Ref. 37, this purely technical element turned out to be a major hurdle for many theoretical studies. The second element of difficulty is that the waves excited at the beginning of the jet in the SDA process then have to propagate over a spatially varying base flow, a particular class of problems reviewed in Ref. 38. Qualitatively, this is similar to the propagation of incident waves along a straight jet stretched by gravity[39] with an additional complication that the base flow has to be found simultaneously with the jet's trajectory. These issues have been addressed in Ref. 40 as part of the present investigation.

The disintegration of a liquid body, in our case, the breakup of a liquid jet into drops, is a particular case from a general class of fluid flows with transitions in the topology of the flow domain. Besides the breakup of jets[41,42] and bridges,[43] this class includes the rupture of films and free liquid sheets,[44,45] coalescence of drops,[46–48] and some other flows. In the context of the present problem, from the viewpoint of practical computations, the main issue is to describe the topological transition without a singularity in the flow field[41,49] as otherwise the singularity, being essentially an unphysical artefact of the modeling, would affect the flow before and after the breakup, as reviewed, for example, in Ref. 49. This aspect of the problem becomes increasingly important as the jet's thickness and hence the size of the drops produced get smaller, eventually becoming comparable with the characteristic length scale associated with the specific physics of breakup which, once incorporated, as in Ref. 43, regularizes the singularities arising in the conventional modeling.

As already mentioned in Sec. I, the flow in the transition zone between the film on the disk and the outgoing jets has not been studied theoretically and it is this element of the process that connects the film and the jet flow and holds the key to the description of the SDA process as a whole.

A qualitative analysis of the results obtained on the elements of the SDA flow outlined above together with the basic estimates for the parameters involved shows that, first, there is a disparity between the frequencies of the waves developing in the film flow on a spinning disk and those required for the waves in the outgoing jets to break the latter into drops of the sizes observed in experiments: the typical size of the drops produced in the SDA process appears to be much smaller than those that the disturbances with frequencies of the waves on the disk would have produced. As a result, one has that the waves in the film, once converted into the waves propagating down the jets, can only modulate the distribution of the drop sizes whilst the drops themselves have to result from disturbances introduced in some other way. It is also worth mentioning here that the local Rayleigh frequency in the jet at a distance from the disk where the drop formation is observed in experiments would have resulted in the drops being much smaller than those observed so the background noise as the source of the drop-forming disturbances can also be ruled out.

The second qualitative conclusion that can be drawn from the published studies is that reproducible results of atomization can be expected in two situations. The first one is where the film is essentially waveless as it enters the transition zone near the disk's edge. This can happen in two cases. First, if the disk is sufficiently small so that the instability of the waveless flow does not have the room to develop into appreciable waves. The second case where one can have a waveless regime is for large disks, where, far away from the axis of rotation, the film becomes so thin that the waves die out as they are damped by the fluid's viscosity. In practical applications, typically, it is the first of these cases (small disk) that is used. Another situation where one can have a reproducible film flow and hence the SDA process with a predictable outcome is where an external frequency is imposed to synchronize the waves in the film and allow the dominating wave to develop. Then, this wave converted into the corresponding wave in the outgoing jets will modulate the flow rate in the latter and hence the distribution of the drop sizes whilst the drop formation itself will be determined by disturbances of another origin.

We will use these preliminary conclusions as a guide in our study.

III. MODELING

Consider the flow resulting from an incompressible Newtonian fluid of density ρ and viscosity μ being continuously

fed, with a constant volumetric flow rate Q, onto a disk of radius R_d spinning at a constant angular velocity $\mathbf{\Omega}$ about a vertical axis coinciding with the disk's axis of symmetry (Fig. 1). The details of how the fluid is introduced into the system remain out of our consideration as we deal with what happens further afield, i.e., outside a small cylinder coaxial with the disk where the liquid is supplied. We will assume that the film flow on the disk's surface is axisymmetric so that, with the azimuthal periodicity of the jets coming out of the disk's rim, we can limit our consideration to a representative sector containing just one jet (Fig. 1). These assumptions correspond to numerous experimental observations for moderate flow rates and rotation velocities where the axial symmetry was observed.[35] In the case of a non-axisymmetric feeding of the fluid near the disk's center, one can observe spiral waves in the central area of the disk which become axisymmetric further away from the axis of rotation.[50]

In the observer's reference frame $Oxyz$ (Fig. 1) where the disk is rotating, the flow velocity $\mathbf{u}$ in the observer's reference frame and pressure p (measured with respect to a constant pressure in the ambient gas) satisfy the Navier-Stokes equations

$$\nabla \cdot \mathbf{u} = 0, \quad \rho\left(\frac{\partial \mathbf{u}}{\partial t} + \mathbf{u} \cdot \nabla \mathbf{u}\right) = \nabla \cdot \mathbf{P} + \rho \mathbf{g}, \tag{1}$$

where $\mathbf{P} = -p\mathbf{I} + \mu\left[\nabla \mathbf{u} + (\nabla \mathbf{u})^T\right]$ is the stress tensor, subject to the no-slip condition on the disk's surface Σ,

$$\mathbf{u} = \mathbf{\Omega} \times \mathbf{r} \qquad \text{for } \mathbf{r} \in \Sigma, \tag{2}$$

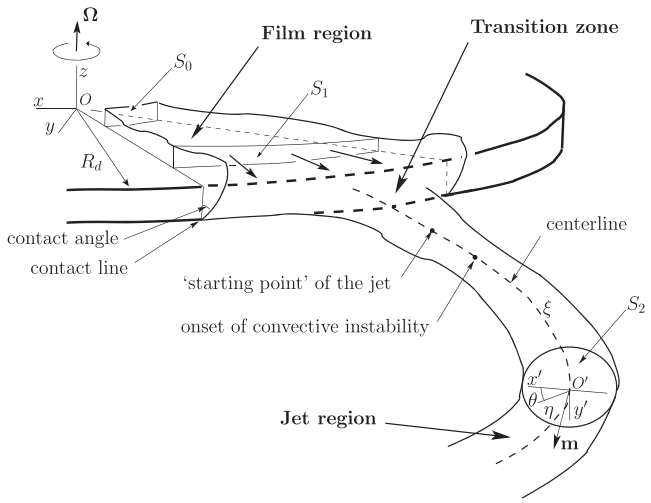

FIG. 1. A sketch of a representative sector of the flow domain containing one jet. The opening angle of the representative sector is determined by the number of jets given by (26) and (27). The subdomain between the entry cross section S_0 and an artificial internal interface S_1 is the "film region"; the subdomain between S_1 and an artificial internal interface S_2 is the "transition zone"; the subdomain further down the jet is the "jet region." The arc length ξ along the jet's centerline together with plane polar coordinates η (the distance from the centerline) and θ (the angle measured from the principal normal to the centerline) in the jet's cross section normal to the centerline forms the local jet-specific non-orthogonal coordinate system. Equations for the spiral jet apply and the ξ-coordinate is measured from the "starting point of the jet" which is located within the transition zone.

and the standard kinematic and dynamic boundary conditions on the free surface S given, respectively, by

$$\frac{\partial f}{\partial t} + \mathbf{u} \cdot \nabla f = 0 \qquad \text{for } \mathbf{r} \in S \tag{3}$$

and

$$-\mathbf{n} \cdot \mathbf{P} = \sigma \mathbf{n} \nabla \cdot \mathbf{n} \qquad \text{for } \mathbf{r} \in S. \tag{4}$$

In the above expressions, $\mathbf{g} = -g\hat{\mathbf{z}}$ is the acceleration due to gravity ($\hat{\mathbf{z}}$ is the basis vector corresponding to the z-coordinate), $\mathbf{r}$ is the radius-vector, $\mathbf{I}$ is the metric tensor, $f(\mathbf{r}, t) = 0$ is the equation of the free surface with the function f to be determined, $\mathbf{n} = \nabla f/|\nabla f|$ is a unit outward normal to the free surface so that $\nabla \cdot \mathbf{n}$ is the mean curvature of the free-surface, and σ is the surface tension of the liquid-gas interface.

At the disk's edge, as the fluid leaves the disk in the form of separate jets, the free surface intersects with the lateral (vertical) side of the disk forming a three-phase contact line (Fig. 1). If the contact line moves, one faces a serious difficulty in the modeling as the standard problem formulation, with the no-slip boundary condition on the solid surface, does not allow for this type of motion. The "moving contact-line problem" has been the subject of intensive research for several decades (see Ref. 49 for a review), with the most detailed model to date and the corresponding experiments[51,52] indicating that the contact angle formed by a free surface and a solid boundary (Fig. 1) cannot be prescribed as an input in the model as it depends on the flow field and, moreover, in an unsteady process, on how the contact line is moving.[53,54] In our study, we consider the contact line to be pinned to the bottom edge of the disk, as shown in Fig. 1, and regard its vertical coordinate z_{cl} as a geometric parameter of the system. The implications of this assumption and the role of z_{cl} are discussed below.

The disparate length and time scales of the problem are a major obstacle in the way of its numerical simulation in a straightforward way as the resources required put it well beyond what can be realistically done with the accuracy for the results to be of practical value. Therefore, one has to adopt an alternative approach and actually use this disparity of scales for the appropriate approximations in different parts of the flow domain. The difficulty is then to match the solutions in different subdomains such that the description of the process as a whole ensures that no valuable information is lost in the exchange between subdomains.

Qualitatively, the flow domain naturally splits into three subdomains: (i) the film region, (ii) the transition zone near the disk's edge, where the film turns into jets leaving the disk, and (iii) the jet region stretching away from the disk, where the drop formation takes place. It should be emphasized here that the distinction between these regions is based on the dynamics of the fluid motion there, not on geometry. This distinction is particularly important in the matching of the flow in the transition zone with the jet region. On the one hand, in order to find the flow in the transition zone, one needs to consider the transition zone together with the "stem" of the jet. On the other hand, to describe the flow in the jet region and the disturbances propagating along the jet, one needs to consider the jet from its natural "starting point" (to be determined) which is located in the jet's "stem" already involved in the description of the transition zone (Fig. 1). This overlapping of the two subdomains

in terms of their dynamics ensures the proper matching of the flow in the two regions.

A. Film region

The film region is located between two coaxial cylindrical surfaces separating it, on the one hand, from the central area of the disk, where the details of how the fluid is introduced into the system are important and the appropriate film flow regime is not yet formed, and, on the other, from the disk's rim, where the flow becomes essentially three-dimensional. In Fig. 1, the cross sections of these cylindrical surfaces with the flow domain of a representative sector containing one jet are shown as S_0 and S_1, respectively. As outlined in Sec. II, the film flow on a spinning disk has been investigated in many studies so that we only need to recapitulate the relevant results from Refs. 26, 27, 35, and 55–61 and present them in a ready-to-use form.

The film flow on a spinning disk is characterized by the following length scales. First, it is (i) the scale R characterizing the flow in the radial direction, which we will take to be the distance from the axis of rotation to S_2 where we will need the inlet conditions for the flow in the transition zone, and then we have (ii) the characteristic film thickness

$$H = \left(\frac{\nu Q}{2\pi\Omega^2 R^2}\right)^{1/3}, \tag{5}$$

where $\nu = \mu/\rho$ is the kinematic viscosity, and, finally, if the film flow is wavy, (iii) a scale characterizing the length of capillary waves developing in the film. The choice of H is such that the dimensionless flow rate of the axisymmetric waveless flow at $r = R$ is equal to one.[35]

In a typical film flow over a spinning disk, the film thickness is small so that the local aspect ratio $\varepsilon(R) \equiv H/R \ll 1$, and an analysis of experimental data carried out in Ref. 35 shows also that the waves can be described in the long-wave approximation, i.e.,[35] $\varepsilon(R)/\kappa \ll 1$, where

$$\kappa = 3^{1/9}\left(\frac{\sigma H}{\rho\Omega^2 R^4}\right)^{1/3}.$$

In this case, the full Navier-Stokes system can be accurately approximated by a set of evolution equations using an approach developed in Ref. 62 for the falling-film flow. In essence, the approach generalizes the Karman-Pohlhausen method known in the boundary-layer theory by utilizing that, as indicated by experiments,[31] the longitudinal velocity profile in the wavy film flow is of the same form as in the waveless flow. The evolution equations derived in Ref. 35 contain two similarity parameters, the film parameter

$$\delta = \frac{3^{11/9}}{45\nu^2}\left(\frac{\rho\Omega^8 R^4 H^{11}}{\sigma}\right)^{1/3} \tag{6}$$

similar to that in the falling film theory[63] and the Eckman number

$$\mathrm{E} = \frac{\nu}{3^{1/6}\Omega H^2}, \tag{7}$$

which characterizes the role of the centrifugal force. The evolution equations tend to those of the falling film theory as $\mathrm{E} \to \infty$. Both δ and E are expressed in terms of the dimensional flow parameters so that, to verify the applicability of the long-wave approximation criterion $\varepsilon/\kappa \ll 1$, we note that

$$\kappa = \left(15\delta\mathrm{E}^2\right)^{-1}. \tag{8}$$

The waveless/steady film flow regime on a spinning disk has been studied in a number of studies.[26,55–57] The solution is found to depend on the velocity profile at the inlet and the Eckman number. As the distance from the axis of rotation increases, the velocity components (u_r, u_θ, u_z) in cylindrical coordinates corresponding to the Cartesian coordinates $Oxyz$ shown in Fig. 1 and the film's thickness h tend to the following asymptotic solution:

$$u_r = \frac{\Omega^2 H^2 r}{\nu}\left[\frac{h_0 z}{H} - \frac{z^2}{2H^2} + O\left(\frac{1}{\mathrm{E}^2}\right)\right], \tag{9}$$

$$u_\theta = \Omega r + \frac{\Omega^2 H^2 r}{\nu}\left[-\frac{2h_0^3 z}{3H} + \frac{h_0 z^3}{3H^3} - \frac{z^4}{12H^4} + O\left(\frac{1}{\mathrm{E}^2}\right)\right], \tag{10}$$

$$u_z = \frac{\Omega^2 H^3}{\nu}\left[\frac{z^3}{3H^3} - \frac{2h_0 z^2}{3H^2} + O\left(\frac{1}{\mathrm{E}^2}\right)\right], \tag{11}$$

$$h = H\left[h_0 + O\left(\frac{1}{\mathrm{E}^2}\right)\right], \tag{12}$$

where $h_0 = 3^{1/3}(r/R)^{-2/3}$ and r is the distance from the axis of rotation. Although, the solution (9)–(12) was derived for large values of the Eckman number, as found in Ref. 57, it gives a good approximation for the flow everywhere except a small region near the axis of rotation where the flow is influenced by the inlet conditions. The maximum value of R for which the film remains waveless depends on δ and E, provided that the fluid is fed onto the disk sufficiently smoothly and axisymmetrically in the inlet area, i.e., between S_0 and the disk's axis of rotation (Fig. 1). For example, as considered in Ref. 64, for $\delta = 0.1$ and $\mathrm{E} = 5$, the maximum radius of the waveless region is about 2.5 times that of the inlet area.

As mentioned in Sec. II, one can also have a waveless regime at large R (for sufficiently large disks) where, after the initial waveless flow followed by a wavy region, the film becomes waveless again as its thickness decreases and the waves are damped by the combined action of viscosity and capillarity. For large R, the film flow on a spinning disk is similar to that of a falling film where, according to Ref. 65, the waves become too small to be measured if $\delta < 0.04$. For the spinning disk flow, this value of δ is the upper bound since the falling film case corresponds to $\mathrm{E} = \infty$ whilst a lower value of E can only stabilize the flow.[60]

In a wavy regime, the problem of finding the film flow becomes considerably more complex. The validity of the approximate evolution system has to be verified by comparing the results of the linear stability analysis of the waveless flow[35] and the corresponding results obtained in the framework of the full Navier-Stokes problem.[58,59] The waveless solution is found to be unstable with respect to low frequency perturbations, i.e., for the dimensionless frequency $\bar{\omega} = \mathrm{E}\kappa\omega/\Omega$ in an interval $(0, \bar{\omega}_n)$, where $\bar{\omega}_n$ is the neutral frequency.[35]

The instability mechanism appears to be similar to that in the falling film problem, where one has only one similarity parameter δ. In the film flow on a disk, the main flow stabilizes as the second similarity parameter, the Eckman number E, decreases.[60] Note that the value of R featuring in the scales and similarity parameters corresponds to the point where the local linear stability analysis is performed.

Similar to the falling film flow,[63,66] the flow over a spinning disk can display a rich set of non-linear waves.[27] Notably and in contrast to the falling film case, the film flow over a spinning disk does not have spatially periodic traveling waves but there are quasiperiodic solutions computed in the framework of an irregular approximation[35] and these solutions are found to be in good agreement with experimental data[27] and the results of transient computations.[64]

As mentioned in Sec. II, for the same flow rate and speed of rotation, there can be many waves corresponding to different frequencies so that, for the wave pattern to be reproducible, the frequency of the waves ω has to be imposed externally. However, even an imposed external frequency does not specify the solution/wave uniquely as, theoretically, there are different waves corresponding to the same frequency. As shown in Refs. 61 and 64, of all solutions, one has to choose the one with the maximum wave speed as it is this wave, labeled "the dominating wave," which is observed in experiments. In the long-wave approximation, the dominating wave is fully specified by three functions, $\bar{h}(\eta)$, $\bar{q}_r(\eta)$, and $\bar{q}_\theta(\eta)$ defined as

$$\bar{h} = \frac{h}{3^{1/3}H}, \quad \bar{q}_r = \frac{\nu}{\Omega^2 H^3 r}\int_0^h u_r\, dz,$$

$$\bar{q}_\theta = 3^{-1/2}\frac{\nu}{\Omega^2 H^3 r}\left(\int_0^h u_\theta\, dz - \Omega r h\right),$$

where $\eta = \bar{\omega}(\alpha\bar{x} - \bar{t})$,

$$\bar{t} = \left(\frac{\rho\Omega^8 R^4 H^5}{\sigma}\right)^{1/3}\frac{t}{3^{4/9}\nu}, \quad \bar{x} = 3^{-1/9}\left(\frac{\rho\Omega^2 R^4}{\sigma H}\right)^{1/3}\log\frac{r}{R} \tag{13}$$

are the appropriately nondimensionalized time t and radius r and α is the inverse speed of the wave. Once the dominating wave solution is found as described in Ref. 35, i.e., one knows functions $\bar{h}(\eta)$, $\bar{q}_r(\eta)$, $\bar{q}_\theta(\eta)$, and α, the components of velocity u_r, u_θ, and u_z can be calculated as

$$u_r = \frac{\Omega^2 H^2 r}{\nu}\cdot\frac{3^{2/3}\bar{q}_r}{\bar{h}}\left(\frac{\bar{z}}{\bar{h}} - \frac{\bar{z}^2}{2\bar{h}^2}\right), \tag{14}$$

$$u_\theta = \frac{\Omega^2 H^2 r}{\nu}\cdot\frac{5\bar{q}_\theta}{4\cdot 3^{1/3}\bar{h}}\left(\frac{2\bar{z}}{\bar{h}} - \frac{\bar{z}^3}{\bar{h}^3} + \frac{\bar{z}^4}{4\bar{h}^4}\right) + \Omega r, \tag{15}$$

$$u_z = \frac{3^{8/9}\Omega^2 H^3}{\nu} \times\left[\frac{\bar{q}_r}{\bar{h}}\left(\frac{\bar{z}^2}{\bar{h}^2} - \frac{\bar{z}^3}{2\bar{h}^3}\right)\frac{\partial\bar{h}}{\partial\bar{x}} - \left(\frac{\bar{z}^2}{\bar{h}^2} - \frac{\bar{z}^3}{3\bar{h}^3}\right)\left(\frac{1}{2}\frac{\partial\bar{q}_r}{\partial\bar{x}} + \kappa\bar{q}_r\right)\right], \tag{16}$$

where $\bar{z} = 3^{-1/3}z/H$ is the non-dimensional vertical coordinate (Fig. 1). It should be noted that, as the last term in (15) indicates, expressions (14)–(16) are for the components of velocity in the observer's reference frame so that, to obtain the corresponding components in the coordinate frame rotating with the disk, the last term on the right-hand side of (15) should be taken out.

Thus, to find the dominating wave solution for a given wave frequency $\bar{\omega}$, one needs, first, to calculate the characteristic film thickness H from (5) and the local values of the similarity parameters δ and E from (6) and (7). Then, it is necessary to compute the eigenfunctions $\bar{h}(\eta)$, $\bar{q}_r(\eta)$, and $\bar{q}_\theta(\eta)$ and the eigenvalue α of the dominating wave. The latter is a rather intricate task as it involves, first, considering the structure of the 3-dimensional manifold $\alpha = f(\delta, \mathrm{E}, \bar{\omega})$ in a 4-dimensional space $(\delta, \mathrm{E}, \bar{\omega}, \alpha)$ as there are a number of eigensolutions/waves corresponding to a given combination of $(\delta, \mathrm{E}, \bar{\omega})$. Second, one should be able to explore this manifold numerically, i.e., to be able to move along it and from one leaf to another, such that it would be possible to compute different eigensolutions/waves for the same $(\delta, \mathrm{E}, \bar{\omega})$ and then determine the one with the smallest α which corresponds to the dominating wave. This second aspect can be addressed by using the invariant embedding method.[35] The gist of this method is as follows.

To be able to move efficiently along a curve $\delta = \delta(l)$, $\mathrm{E} = \mathrm{E}(l)$, $\bar{\omega} = \bar{\omega}(l)$, and $\alpha = \alpha(l)$ in the solution manifold, one can differentiate the ordinary differential equations for periodic functions $\bar{h}(\eta)$, $\bar{q}_r(\eta)$, and $\bar{q}_\theta(\eta)$ along this curve, i.e., with respect to l, to arrive at a system of partial differential equations with respect to η and l. The solution of this system is looked for in the form of a truncated complex Fourier series with the base functions depending on η. After substituting this solution in the system and collecting the coefficients of the exponential terms, we arrive at a system of ordinary differential equations for the Fourier coefficients depending on l whereas the periodic boundary conditions for the functions $\bar{h}(\eta)$, $\bar{q}_r(\eta)$, and $\bar{q}_\theta(\eta)$ are satisfied. The derived system can be solved using a standard method, for example, the Adams-Bashforth method of second order. Treating the obtained solution as the initial approximation, it can then be corrected at any value of l by using the Newton-Raphson method. By varying the curves on the solution manifold—and by-passing the singularities—one can compute all dominating waves provided that one knows at least one solution/point on the manifold to start from. As this starting point, one can take, for example, a known falling film solution given that it is the limit of the film on the disk solution as $\mathrm{E} \to \infty$. If the similarity parameters δ and E are kept constant and $l = \bar{\omega}$, one has what is referred to as "families" of quasi-steady periodic waves. The details of the use of the invariant embedding method can be found elsewhere.[35]

It is noteworthy that computing just the dominating waves requires by far less computer resources than mapping the entire three-dimensional manifold.

Once the dominating wave is found, one can use the film thickness $\bar{h}$ obtained as part of the solution and the velocity profile (14)–(16) as the inlet conditions at S_1. As already mentioned, in (14)–(16), we drop the last term on the right-hand side of (15) to have the azimuthal velocity component in the rotating frame.

B. Jet region

As the film disintegrates into jets, each of them can be described separately as a representative jet corresponding to the appropriate sector of the film (Fig. 1) in a coordinate frame rotating with the jet. As we will see below, the angular velocity of this frame, denoted as $\mathbf{\Omega}_j = \Omega_j \hat{\mathbf{z}}$, differs from the angular velocity of the disk $\mathbf{\Omega}$. For the description of the jet and then for the drop formation process, we essentially only need to recap, summarize, and adjust the relevant results from Refs. 37 and 40.

In a free jet, unlike a pipe flow, there are no tangential forces on the jet's free boundary to sustain the non-uniform velocity profile across the jet. As a result, within a few jet diameters away from the disk's rim, viscosity unifies the velocity profile so that in the subsequent dynamics viscosity becomes negligible and the fluid behaves as inviscid. This qualitative consideration can be easily verified numerically by computing the flow in the transition zone with almost any "soft" boundary conditions at S_2; the proper way of finding the solution in the transition zone is describe below. Viscosity becomes important again further down the jet, where the free-surface disturbances propagating along the jet enter the nonlinear regime and in the capillary breakup of the jet resulting in the formation of drops.

Thus, in the coordinate frame rotating with the jet, one has to solve

$$\nabla \cdot \mathbf{u} = 0, \quad \frac{\partial \mathbf{u}}{\partial t} + \mathbf{u} \cdot \nabla \mathbf{u} = -\frac{1}{\rho}\nabla p + \mathbf{g} - 2\mathbf{\Omega}_j \times \mathbf{u} - \mathbf{\Omega}_j \times (\mathbf{\Omega}_j \times \mathbf{r}), \tag{17}$$

where the last term on the right-hand side is the centrifugal force and the preceding term is the Coriolis force, subject to the standard kinematic condition (3) and the dynamic boundary condition (4) which now takes the form

$$p = \sigma \nabla \cdot \mathbf{n}. \tag{18}$$

Since in practice for a jet the ratio of the cross sectional dimension H to the characteristic length scale along the jet L is invariably small, one can use this ratio as a small parameter and, to simplify the problem, consider the slender-jet approximation as $H/L \to 0$ to obtain equations for the jet's trajectory and the base flow.[37] If $Ox_jy_jz_j$ is the Cartesian coordinate system rotating with the jet, with the z-axis directed along the axis of rotation of the disk, so that $x_j = X(\xi)$, $y_j = Y(\xi)$, and $z_j = Z(\xi)$ are the (time-independent) dimensionless equations describing the shape of the jet's centerline (i.e., trajectory), where ξ is the arc length along it, the functions X, Y, and Z satisfy the following ordinary differential equations:[37]

$$\left(u_{\xi,0}^2 - \frac{u_{\xi,0}^{1/2}}{\mathrm{We}_j Q_1^{1/2}}\right)(X'^2 + Y'^2 + Z'^2) + \frac{1}{\mathrm{Fr}_j^2}Z' + \frac{2}{\mathrm{Rb}_j}u_{\xi,0}(X'Y'' - Y'X'') - \frac{1}{\mathrm{Rb}_j^2}(XX'' + YY'') = 0, \tag{19}$$

$$\frac{1}{\mathrm{Fr}_j^2}(X'Y'' - Y'X'') + \frac{2}{\mathrm{Rb}_j}u_{\xi,0}[X'(Z'X'' - X'Z'') - Y'(Y'Z'' - Z'Y'')] - \frac{1}{\mathrm{Rb}_j^2}[X(Y'Z'' - Z'Y'') + Y(Z'X'' - X'Z'')] = 0, \tag{20}$$

$$X'^2 + Y'^2 + Z'^2 = 1, \tag{21}$$

where primes denote differentiation with respect to ξ, the velocity along the jet $u_{\xi,0}(X, Y, Z)$ (the subscript 0 refers to the base/unperturbed flow) is specified by

$$u_{\xi,0}^2 + \frac{2}{\mathrm{We}_j Q_1^{1/2}}u_\xi^{1/2} + \frac{2}{\mathrm{Fr}_j^2}Z - \frac{1}{\mathrm{Rb}_j^2}(X^2 + Y^2) + Q_2 = 0, \tag{22}$$

and the jet-specific Weber number, We_j, Froude number, Fr_j, and Rossby number, Rb_j, are defined by

$$\mathrm{We}_j = \frac{\rho U^2 H}{\sigma}, \quad \mathrm{Fr}_j = \frac{U}{\sqrt{gL}}, \quad \mathrm{Rb}_j = \frac{U}{\Omega_j L},$$

where U is the characteristic velocity. Constants Q_1 and Q_2 are determined by specifying the volumetric flow rate (which is equal to πQ_1) and the longitudinal velocity of the fluid (uniform across the jet) at one point on the jet's trajectory. The jet's radius, h_0, is obviously given by $h_0 = \sqrt{Q_1/u_{\xi,0}}$.

Note that the above equations have been derived by considering a waveless solution as it can be shown[37] that, in the slender-jet approximation, there are no waves with wavelengths on the scale of the radius of curvature of the jet's trajectory and the motion of the jet as a whole can be caused only by variations in the inlet conditions.

For matching with the solution in the transition zone, we also need the equations for local peristaltic waves. In the slender-jet approximation, such waves have the characteristic length scale much larger than the jet's cross sectional scale but much smaller than the radius of curvature of the jet's trajectory. As a result, the equations describing these waves are, to leading order in the slenderness parameter H/L as $H/L \to 0$, the same as for a straight jet,[37,67]

$$\frac{\partial h}{\partial \bar{t}} + u_\xi \frac{\partial h}{\partial \bar{\xi}} + \frac{h}{2}\frac{\partial u_\xi}{\partial \bar{\xi}} = 0, \quad \frac{\partial u_\xi}{\partial \bar{t}} + u_\xi \frac{\partial u_\xi}{\partial \bar{\xi}} + \frac{1}{\mathrm{We}_j}\frac{\partial}{\partial \bar{\xi}}\left(\frac{1}{h}\right) = 0, \tag{23}$$

where h is the radius of the (circular) cross section of the jet and $\bar{t}$, $\bar{\xi}$ are the appropriately scaled[37] time and the arc length. It should be noted here that in deriving (23), the assumption that, to leading order in H/L as $H/L \to 0$, the longitudinal velocity u_ξ is uniform across the jet, once used in the continuity equation, makes it possible to express the radial component of velocity u_η in terms of u_ξ as

$$u_\eta = -\frac{\eta}{2}\frac{\partial u_\xi}{\partial \bar{\xi}}, \tag{24}$$

where η is the distance from the centerline in the normal cross section to it (Fig. 1), whilst the pressure in the jet is, again to leading order in H/L, the capillary pressure coming only from the cross sectional curvature,

$$p = \frac{1}{h}. \tag{25}$$

We will need (24) and (25) later, in the matching conditions linking the flow in the transition zone and the jet region. It should be emphasized here that Eqs. (23) are *local*; for the analysis of the wave propagation on the spatially varying base flow, we need a different mathematical approach and use the results of Ref. 40.

Equations (23) are evolutionary and require conditions only at the inlet cross section S_2. On their own, Eqs. (23) can

be solved using, for example, a finite-difference scheme with the temporal step sufficiently small compared with the spatial one to ensure the code's accuracy.

C. Unified scaling and similarity parameters for the entire problem

After using asymptotic methods and the appropriate non-dimensionalisation in the film and the jet regions to simplify the problems there, we need to go back to the dimensional form of the (simplified) equations in these regions and the full Navier-Stokes equations in the transition zone to introduce a unified non-dimensionalisation throughout the whole SDA problem. This will give us the corresponding non-dimensional similarity parameters that fully specify the process as a whole and, as one would expect, involve the characteristics of both the film and the jet flow regions. It is these parameters that would feature in an experimental mapping of the flow regimes.

In dimensional terms, we have the following set of parameters: ρ, μ, σ, R_d, Q, Ω, g, $z_{\rm cl}$, and ω, where, as previously discussed, ω is the imposed frequency of the waves in the film region if the disk is large enough for the waves to develop and be taken into account. The flow is also characterized by the total number of jets that go out, $n_{\rm jet}$. This number is specified by the above parameters and finding this dependence theoretically is part of the ongoing research into the SDA. In the present study, we will use an empirical formula determined experimentally by Frost,[3] who found that if one takes, in our notation,

$$n = 0.78\left(\frac{\rho\Omega R_d^2}{\mu}\right)^{0.93}\left(\frac{\mu^2}{\rho\sigma R_d}\right)^{0.44}, \tag{26}$$

then the integer closest to it will give an accurate prediction for the number of jets. Thus, one can use

$$n_{\rm jet} = [n + 0.5], \tag{27}$$

where n is taken from (26) and the square brackets denote the integer part. Recent experiments[5,6] confirmed the accuracy of (26) and (27), and we will use this empirical result below.

In making the problem in the transition zone non-dimensional, it is convenient to use as scales for the length, velocity, time, and pressure the following quantities:

$$H = \left(\frac{\mu Q}{2\pi\rho\Omega^2 R_d^2}\right)^{1/3}, \quad U = \frac{Q}{n_{\rm jet}\pi H^2} = \frac{1}{n_{\rm jet}}\left(\frac{4Q\rho^2\Omega^4 R_d^4}{\pi\mu^2}\right)^{1/3},$$
$$T = \frac{H}{U} = \frac{n_{\rm jet}\mu}{2\rho\Omega^2 R_d^2}, \quad P = \rho U^2 = \frac{1}{n_{\rm jet}^2}\left(\frac{4Q\rho^{7/2}\Omega^4 R_d^4}{\pi\mu^2}\right)^{2/3}. \tag{28}$$

Note that we have to introduce the length scale characteristic of the film whilst the velocity (and hence the time) scale is that characteristic of the jet. The resulting problem will include the following non-dimensional similarity parameters:

$$\mathrm{Re} = \frac{\rho UH}{\mu} = \frac{1}{n_{\rm jet}}\left(\frac{2^{1/2}\rho^2 Q\Omega R_d}{\pi\mu^2}\right)^{2/3},$$
$$\mathrm{We} = \frac{\rho U^2 H}{\sigma} = \frac{2\rho^2 Q\Omega^2 R_d^2}{\pi n_{\rm jet}^2\mu\sigma}, \tag{29}$$

$$\mathrm{Fr} = \frac{U}{\sqrt{gH}} = \frac{1}{n_{\rm jet}g^{1/2}}\left(\frac{Q}{\pi}\right)^{11/6}\left(\frac{\mu}{2\rho\Omega^2 R_d^2}\right)^{5/6},$$

$$R_d^* = \frac{R_d}{H} = \left(\frac{2\pi\rho\Omega^2 R_d^5}{\mu Q}\right)^{1/3}, \quad z_{\rm cl}^* = \frac{z_{\rm cl}}{H} = z_{\rm cl}\left(\frac{2\pi\rho\Omega^2 R_d^2}{\mu Q}\right)^{1/3}.$$

The Rossby number characterizing the Coriolis and centrifugal forces is then given by

$$\mathrm{Rb} = \frac{U}{\Omega H} = R_d^*\sqrt{\frac{2\mathrm{Re}}{n_{\rm jet}}}. \tag{30}$$

Note that the above similarity parameters are needed simply to identify the case one is dealing with in the parameter space as no simplifications in the transition zone are possible. Alternatively, one can identify the case by using in the film region

$$\omega^* = \omega T = \frac{\omega\mu n_{\rm jet}}{2\rho\Omega^2 R_d^2}, \qquad \delta = \frac{3^{11/9}}{45\nu^2}\left(\frac{\rho\Omega^8 R_d^4 H^{11}}{\sigma}\right)^{1/3},$$
$$\mathrm{E} = \frac{\nu}{3^{1/6}\Omega H^2},$$

which make it possible to check the results against those published for the spinning disk flow and, separately, the similarity parameters in the jet region as in Ref. 37.

IV. TRANSITION ZONE AND MATCHING CONDITIONS

A. Transition zone

In the transition zone between the film and the outgoing jet, i.e., between S_1 and S_2 in Fig. 1, we have a three-dimensional, generally, unsteady free-boundary problem with no features that would have made possible any analytic simplifications. Therefore, it has to be solved in full using an appropriate numerical method focussed on accurately tracking the free surface evolution. To solve the problem, a computational platform based on the finite-element method[68] has been developed. The platform is essentially an extension to three dimensions of the numerical framework described in detail in Ref. 69. The detailed finite-element discretization for a three-dimensional free-surface flow can also be found in Ref. 70.

The developed code uses an Arbitrary Lagrangian-Eulerian (ALE) approach, known as the method of spines and described in detail in Ref. 71, so that the free-surface dynamics can be captured with high accuracy. The choice of this approach, as opposed to the one involving an unstructured mesh, is dictated by the need to optimize the computations and hence make the problem tractable; the price is the effort one has to invest in designing the mesh that is both flexible and robust. The mesh design used in the platform involves two main elements: (i) the mesh for the outgoing jet with the wedge-like prism elements adjacent to the jet's "baseline," a smooth line passing near the jet's centre, combined with parallelepipedal elements further away from the baseline and (ii) the mesh in the region along the disk's rim and its upper surface where parallelepipedal elements are used (see Fig. 2). The structured mesh design allows for the grading of the mesh to capture details of

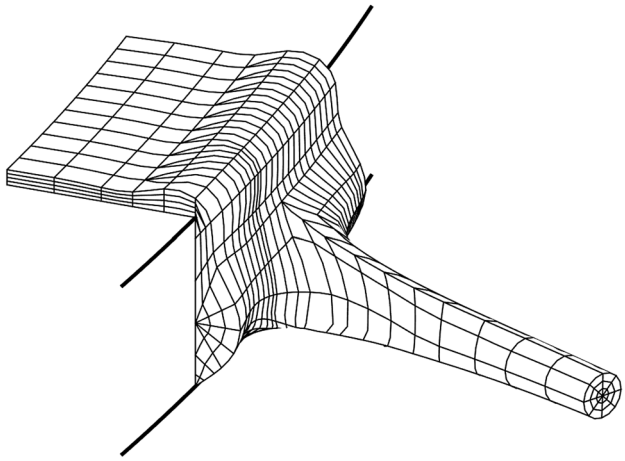

FIG. 2. Sketch illustrating the mesh structure.

the flow where higher accuracy is required, in particular, where the flow along the disk's rim turns into the jet flow, and at the same time keeps the number of elements to a minimum. In each element, the flow velocity is approximated quadratically and pressure linearly to satisfy the Ladyzenskaya-Babuska-Brezzi condition.[72] A typical mesh used in our computations involved 1208 elements corresponding to 32 443 unknowns. The mesh parameters and the number of elements have been varied to ensure mesh-independence of the calculation results. The spatial discretization of the problem produces a system of nonlinear differential algebraic equations of index two which are then solved using the second-order backward differentiation formula (BDF2) with a time step automatically adapting to capture the temporal scale characteristic to each instance. The resulting equations are solved at each time step using Newton's method.

B. Matching conditions

In order to simulate the SDA process as a whole, the solutions in three regions, i.e., the film region, the jet region, and the transition zone, have to be matched at the interfaces between them shown in Fig. 1 as S_1 and S_2. At S_1, the matching is relatively straightforward: the shape and the orientation of S_1 are known as S_1 is simply a cross section of the film by a cylindrical surface coaxial with the axis of rotation of the disk. The boundary conditions one has to set there for the Navier-Stokes equations in the transition zone are the velocity distribution and the film thickness. For the waveless film flow, these conditions are fully specified by (9)–(12), whilst for the wavy regime one needs to solve the eigenvalue problem outlined above and then calculate the velocity distribution from (14)–(16), where, as already mentioned, u_θ must be taken in the rotating coordinate frame. The only requirement that needs to be satisfied and numerically verified is that S_1 is located sufficiently far upstream for the upstream influence of the disk's edge on the film flow, and hence the influence of the location of S_1 on the results, to be negligible.

Note that the inlet conditions at S_1 should be consistent with the flow parameters in the transition zone. An example of the opposite can be found in Ref. 73, where the inlet conditions obtained in Ref. 74 in the lubrication approximation, i.e., at zero Reynolds number, have been used as an input in Fluent's volume-of-fluid software at finite/large Reynolds numbers which correspond to a wavy flow the authors themselves referred to as "turbulent."

The matching conditions at the interface between the transition zone and the jet region (S_2 in Fig. 1 referred to as the "outlet") are more intricate. First, we do not know *a priori* neither the spatial location nor the orientation of S_2 with respect to the disk. Second, the flows in the transition zone, where the full Navier-Stokes equations are used, and the jet region, where for matching purposes we use Eqs. (23), are described by essentially different systems of equations involving different numbers of dependent and independent variables and requiring a different number of boundary conditions and numerical methods for their solution. It should be emphasized here that Eqs. (23) in the jet region are needed only for the matching, i.e., to find the solution in the transition zone. The Navier-Stokes equations in the transition zone need boundary conditions at S_2, which is an artificial boundary, and hence the conditions there should have no upstream effect on the flow, and it is for this purpose that we need evolutionary equations (23) which, with the matching described below, will accept the information coming from the transition zone without a backward influence.

As the jet gradually forms, stemming from the transition zone and extending further away from the disk's rim, the fluid's viscosity acts as a unifier of the velocity profile across the jet and, together with the surface tension, creates a circular cross section as the non-axisymmetric disturbances die out. All this can be observed in a numerical experiment if one computes the flow in the transition zone with almost any "soft" boundary conditions at the outlet and moves this outlet further and further away from the disk; then, one can see how an almost axisymmetric jet with an approximately uniform velocity profile across it forms already a few jet diameters away from the disk. Such dynamics ensures that the flows in the transition zone and in the jet region, where the velocity is assumed to be uniform and the cross section circular, can be matched and dictates that S_2 has to be located sufficiently far away from the disk's rim. As with S_1, the limitations on how far it can be located come from the available computer resources as solving the 3D unsteady free-boundary problem for the Navier-Stokes equations in the transition zone becomes prohibitively costly computationally if S_2 is too far away.

1. Matching conditions specifying the location and orientation of S_2

To find the jet's trajectory/centerline, we need to consider a steady (waveless) flow with the same flow rate and angular velocity of rotation as in the wavy flow to be studied subsequently. The obtained centerline can then be used as the "baseline" for the mesh in the transition zone and the plane normal to it will be that of S_2.

In the frame rotating with angular velocity $\mathbf{\Omega}_j$, the centerline of the jet is described by Eqs. (19)–(22) where the solution is specified by 7 constants, namely, the starting point $X(0)$, $Y(0)$, $Z(0)$, the direction of the trajectory at this point determined by derivatives $X'(0)$, $Y'(0)$, $Z'(0)$ of which, given (21),

only two are independent, and, finally, two constants, Q_1, Q_2, featuring in (19)–(22). Given the azimuthal periodicity of the film flow on the disk, one can specify the sector with a representative jet (see Fig. 1) arbitrarily with respect to the jet itself, and it is convenient to choose it such that azimuthally the starting point of the centerline is in the middle of it. This gives one constraint linking $X(0)$ and $Y(0)$.

As another condition to specify $X(0)$ and $Y(0)$, we can choose the distance (in the disk's plane) from the axis of rotation to where the jet's trajectory begins, $D(0) = \left(X^2(0) + Y^2(0)\right)^{1/2}$. This is a nontrivial point worth a comment. Equations (19)–(22) for the jet's trajectory and the distribution of the longitudinal velocity, together with $h_0 = \sqrt{Q_1/u_{\xi,0}}$ and (24) and (25), which have the same form for the base flow as for the perturbed flow, describe how the fluid behaves in the jet whilst the fluid motion in the transition zone gradually evolves from the film flow to the jet flow. Therefore, there exists a minimal distance from the disk's rim after which the results of (19)–(22) apply. An attempt to start the jet from a point located closer to the disk than this distance would not succeed as it will be impossible to satisfy all conditions (discussed below) needed to match the jet's "stem" in the transition zone with the jet itself. Mathematically, this comes from the value of the expression in the first bracket of (19) being bounded from below for the inertia-dominated jet to exist. In practice, it is convenient to take $D(0)$ well above the minimal possible value and, after finding the parameters of the jet's trajectory, use Eqs. (19)–(22) backwards to find the point where the jet actually starts. We will refer to it as the "starting point of the jet" (Fig. 1).

There is one additional degree of freedom that has to be added to the 5 that remain after $X(0)$ and $Y(0)$ have been fixed by using the above conditions. One has no reason to expect that the angular velocity with which the jet as a whole rotates $\mathbf{\Omega}_j$ should be the same as the angular velocity of the disk $\mathbf{\Omega}$. Then, in the reference frame rotating with the jet, the disk will be rotating with the angular velocity $\Delta\mathbf{\Omega} = \mathbf{\Omega} - \mathbf{\Omega}_j$ whose magnitude becomes a parameter to be determined. The angular velocity $\Delta\mathbf{\Omega}$ will affect the flow in the representative sector via the no-slip condition on the disk's surface and the inlet condition at S_1.

The cross section S_2 where we need to do the matching is, by definition, normal to the jet's centerline, and the first two of the 6 conditions that we need come from the requirement that, as far as the flow in the jet's "stem" growing from the transition zone is concerned, the centerline we are looking for is at the center of S_2. This means that, in a local plane Cartesian frame $O'x'y'$ in the normal cross section with the origin on the centerline (Fig. 1), the geometric static moments of S_2 with respect to the coordinate axes are zero,

$$\int_0^{2\pi} \cos\theta\, d\theta \int_0^{h(\theta)} \eta^2\, d\eta = \int_0^{2\pi} \sin\theta\, d\theta \int_0^{h(\theta)} \eta^2\, d\eta = 0.$$

Then, we have three conditions coming from the requirement that, in a steady flow, the velocity $\mathbf{u}$ computed in the transition zone and evaluated at S_2 must be the one that features in Eqs. (19)–(22) of the jet, namely,

$$\frac{1}{S_2}\iint_{S_2} \mathbf{u}\cdot\mathbf{m}\, dS = u_{\xi,0}, \qquad \iint_{S_2} \mathbf{u}\cdot\hat{\mathbf{x}}'\, dS = \iint_{S_2} \mathbf{u}\cdot\hat{\mathbf{y}}'\, dS = 0,$$

where $\hat{\mathbf{x}}'$ and $\hat{\mathbf{y}}'$ are the basis vectors of $O'x'y'$ and $\mathbf{m} = \hat{\mathbf{x}}' \times \hat{\mathbf{y}}'$. For definiteness, it is convenient to align $O'x'$ and $O'y'$ with the normal and binormal to the centerline, though in the above condition, any orientation of these axes can be used.

Finally, from the physical meaning of Q_1,[37] we have

$$\iint_{S_2} \mathbf{u}\cdot\mathbf{m}\, dS = \pi Q_1.$$

With the centerline for the waveless flow specified by the above conditions, we also need to formulate at S_2, for both the waveless and the wavy flow, the matching conditions for the flow in the transition zone and the jet region.

2. Matching the flows across S_2

Since S_2 is an artificial interface, the matching conditions at S_2 have to be essentially the conditions of continuity and smoothness across S_2 of the flow variables. For convenience, we will mark the variables with superscripts – and + corresponding to the limits as one approaches S_2 from the transition zone and from the jet region, respectively.

The subtlety in formulating and computationally implementing the matching conditions for the flow is that the flows in the transition zone and in the jet region are described by different equations and hence require different number of conditions and different numerical methods for their solutions. In the transition zone, we have the full 3D Navier-Stokes equations which require three conditions, say, on the components of velocity, and the fully prescribed boundary ∂S_2 of the cross section S_2, i.e., the function $h^-(\theta)$. On the other hand, in the jet region, we have a 1D evolutionary model (23), which needs only two initial values of h^+ and u_ξ^+. In numerical terms, we have N inner nodes in S_2 and N_B boundary nodes on ∂S_2, where we need $3N + N_B$ conditions for the finite-element method in the transition zone and we also need 2 conditions for the finite difference scheme solving (23).

As the first step, from the full set of continuity conditions at S_2, which includes the continuity of all flow variables and their derivatives with respect to ξ, we can take the subset involving only h^+ and u_ξ^+, i.e., the radius of the circular cross section and the velocity involved in (23),

$$u_\xi^- = u_\xi^+, \qquad u_\eta^- = -\frac{\eta}{2}\frac{\partial u_\xi^+}{\partial \xi}, \qquad u_\theta^- = 0, \qquad \frac{\partial u_\xi^-}{\partial \xi} = \frac{\partial u_\xi^+}{\partial \xi} \qquad (\mathbf{r} \in S_2), \tag{31}$$

$$h^- = h^+, \qquad \frac{\partial h^-}{\partial \xi} = \frac{\partial h^+}{\partial \xi} \qquad (\mathbf{r} \in \partial S_2). \tag{32}$$

In the second condition in (31), we used (24) for the radial component of velocity in the jet region. Systems (31) and (32) obviously massively overspecify the solutions, and we need to replace one condition on S_2 and one condition on its boundary ∂S_2 with the corresponding integral form of the condition. It is convenient to replace the first conditions in (31) and (32) with

$$\frac{1}{S_2}\iint\limits_{S_2}\mathbf{u}^-\cdot\mathbf{m}\,dS = u_\xi^+, \qquad \int\limits_0^{2\pi} d\theta \int\limits_0^{h^-}\eta\,d\eta = \pi(h^+)^2, \quad (33)$$

respectively. These conditions together with the remaining conditions in (31) and (32) fully specify the solution. It should be noted here that the derivative with respect to ξ in these conditions is, in general, not the derivative in the direction normal to S_2 as the local coordinate system (ξ, η, θ) shown in Fig. 1 is not orthogonal if the torsion of the jet's centerline is nonzero.[37] The corresponding error is proportional to the jet's thickness and appears to be within the computational accuracy so that, for simplicity, one can use the derivatives normal to S_2.

Since in the transition zone we use the finite-element method, it is more convenient to reformulate the conditions involving derivatives of velocities in terms of stresses that appear naturally in the finite-element implementation of the Navier-Stokes equations. Given that, as all flow variables, the pressure is continuous across S_2 and taking into account (25) in the jet region, we can replace the second condition in (31) with

$$-p^- + 2\mu\frac{\partial u_\xi^-}{\partial\xi} = -\frac{\sigma}{h^+} + 2\mu\frac{\partial u_\xi^+}{\partial\xi} \qquad (\mathbf{r}\in S_2). \quad (34)$$

By combining the first two conditions in (31) and using that in the jet region u_ξ^+ is independent of η, we obtain

$$\frac{\partial u_\xi^-}{\partial\eta} + \frac{\partial u_\eta^-}{\partial\xi} = -\frac{\eta}{2}\frac{\partial^2 u_\xi^+}{\partial\xi^2} \qquad (\mathbf{r}\in S_2). \quad (35)$$

The last conditions in (31) and (32) stay as they are,

$$u_\theta^- = 0 \qquad (\mathbf{r}\in S_2), \qquad \frac{\partial h^-}{\partial\xi} = \frac{\partial h^+}{\partial\xi} \qquad (\mathbf{r}\in\partial S_2). \quad (36)$$

Conditions (33)–(36) when implemented numerically result in $3N + N_B + 2$ conditions as required.

V. DISTURBANCES IN THE JET AND DROP FORMATION

The role of the matching conditions described above is twofold. First, they make it possible to determine the flow in the transition zone without a backward effect of the artificial outlet boundary S_2 and, in particular, examine the effect of the disk's edge on the flow. Second, they simultaneously allow one to determine the parameters of the trajectory and the base flow in the outgoing jet. This last aspect is particularly important as now, to analyze the propagation of disturbances along the jet and the drop formation that follows, one can deal with the jet separately using the mathematical framework developed in Ref. 37 for a generic spiralling jet. The region between the "starting point of the jet" and S_2 (Fig. 1) is where the transition zone, with the flow described by the 3D Navier-Stokes equations, and the equations for the spiralling jet of an inviscid fluid derived in Ref. 37 overlap. Quantitative comparison of solutions obtained using these two sets of equations shows that, in the waveless regime, the difference between them does not exceed 3% which should be regarded as a very satisfactory outcome.

The key question regarding the SDA process is the origin of disturbances which determine the size of the drops produced as the result. The conjecture that the drops emerge as a result of the capillary instability triggered by the background noise along the jet has to be discarded. Indeed, in a spiralling jet, we have that the fluid velocity increases and the jet's radius correspondingly decreases as the distance from the "starting point of the jet" increases so that, should the jet's breakup be the result of the background noise and determined locally, the size of the resulting drops would scale with the cube of the jet's unperturbed radius evaluated near the point where the drops form. However, by analyzing experimental data, one can see that the drops observed in experiments are considerably larger than what the local stability analysis would predict. The breakup due to the wave generated by the recoiling tip of the jet suggested by Wang and co-workers[73] leads to even smaller drops than those resulting from the local Rayleigh instability. On the other hand, the experimentally observed drops are much smaller than those which would correspond to the disturbances in the jet resulting from the long waves in the film on the spinning disk. The frequency associated with the angular velocity of rotation is also too low to be responsible for the drops resulting from the atomization process.

The source of disturbances left to be examined is the noise due to the disk's vibration and other imperfections of the atomizer, e.g., the noise of the motor. Experiments[75,76] show that indeed the spinning disk atomizer generates an entire spectrum of uncontrollable parasitic vibrations and the disturbances they create must be considered as incident with regard to the jet. Then, as considered below, these disturbances can trigger convective instability in the jet as soon as the jet flow becomes convectively unstable. The wavelength of these disturbances will increase as they propagate along the jet whose radius varies as the distance from the jet's starting point increases.[40] This suggests that the incident disturbances coming from the disk would lead to larger drops than those resulting from the local stability analysis. The dynamics of the incident waves propagating along a spiralling jet and the resulting drop formation have been analyzed in Ref. 40, so here we only need to adjust the obtained results to our problem.

The dispersion equation for the linear waves in a spiralling jet has the form[40]

$$(ku_{\xi,0}-\omega)^2 - \frac{k^2}{2\mathrm{We}\,h_0}(h_0^2k^2-1) = 0, \quad (37)$$

where k is the wavenumber, ω is the frequency of the waves, $u_{\xi,0}$ is the velocity of the base flow satisfying (19)–(22), and $h_0 = \sqrt{Q_1/u_{\xi,0}}$ is the unperturbed radius of the jet. For the spatially propagating waves, we regard ω as real and $k = k_r + ik_i$ as complex so that (37) can be written down as two equations

$$(k_ru_{\xi,0}-\omega)^2 - (k_iu_{\xi,0})^2 - \frac{1}{2\mathrm{We}h_0}\left[h_0^2\left((k_r^2-k_i^2)^2-(2k_rk_i)^2\right)-(k_r^2-k_i^2)\right] = 0,$$

$$2k_iu_{\xi,0}(k_ru_{\xi,0}-\omega) - \frac{1}{\mathrm{We}h_0}\left[2k_rk_ih_0^2(k_r^2-k_i^2)-k_rk_i\right] = 0$$

and, for $k_rk_i \neq 0$, the last equation takes the form

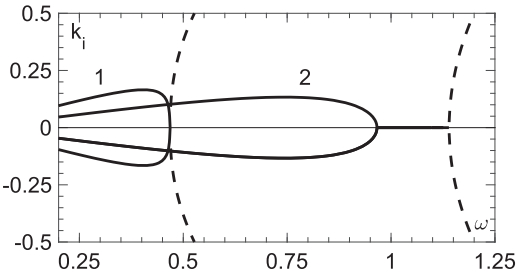

FIG. 3. The phase diagram showing the dependence of the imaginary part of the wavenumber (corresponding to the conjugate roots of the dispersion equation) on the wave frequency. The solid lines correspond to the physically meaningful and the dashed lines to the spurious solutions. As one moves closer to the starting point of the jet, the shape of the spurious (dashed) branch in the phase diagram moves from its generic position toward the loop in the real one (2), and the touching of the two branches (1) corresponds to the lowest velocity and the closest point to the onset of the jet where one has convective instability.

$$k_i^2 = k_r^2 - \frac{1}{2h_0^2}\left[2\mathrm{We}h_0 u_{\xi,0}\left(u_{\xi,0} - \frac{\omega}{k_r}\right) + 1\right].$$

In order to adjust the method developed in Ref. 40 to the SDA problem, it is necessary to determine where the convective instability is triggered, i.e., to identify what should be considered as the starting point for the disturbances. This can be done by considering the phase diagram showing the dependence of the imaginary part of the wavenumber k_i on ω at different distances from the starting point of the jet. The generic shape of this diagram is shown as curve 2 in Fig. 3. We have that it consists of a part (shown as a solid line) with a local minimum corresponding to the spatially fastest growing wave and a spurious part shown as a dashed line. As we move closer to the starting point of the jet, i.e., vary $u_{\xi,0}$ accordingly, the segment along the ω-axis corresponding to neutral stability shrinks and eventually vanishes completely so that the spurious part touches the meaningful one (curve 1, Fig. 3). This point located 2–3 jet diameters from the starting point of the jet (Fig. 1) can be regarded as where convective instability is triggered. The fastest spatially growing wave at this point can be determined by taking the frequency corresponding to the minimum of k_i at this point. Then, following the approach of Ref. 40, one can consider the evolution of this wave, first, in the linear regime and, then, feeding the results of the linear analysis into a full-scale finite-element code accounting for the fluid's viscosity as well as inertia and capillarity, follow the disturbances as they result in the breakup of the jet. Essentially, once the starting point of the disturbances and the wave frequency corresponding to the spatially fastest growing wave are identified, one can apply the approach and use the code developed in Ref. 40. Since the magnitude of the disturbances coming from the disk vibration and triggering convective instability is not known, we have to regard it as a free parameter which will parameterize our results.

VI. SIMULATION RESULTS

The similarity parameters (29) formally specify a multi-dimensional parameter space. Mapping this space in terms of atomization regimes is a very labor-intensive task. Another disincentive here is that in practice the similarity parameters cannot be varied independently so that a variation of the operational parameters, Q and $\mathbf{\Omega}$, leads to variations in several similarity parameters and hence the result would be a curve in this multi-dimensional parameters space. The same applies even to a greater extent to variations of the physical properties of the fluid which themselves cannot be varied independently. Therefore, to illustrate how the method described in Secs. III–V works and the role played by the operational parameters, we examine how the variation of these parameters from some base case influences the SDA flow. Largely qualitative, this approach has an advantage that the results could be put to immediate practical use.

A. Atomization from a waveless film (small disk)

As mentioned in Secs. II and III, the film flow on a spinning disk can be essentially waveless close to the axis of rotation (i.e., for small disks), where the instability has not yet developed into a full-scale nonlinear wave pattern, or far away from the axis (i.e., for very large disks), where the film thickness becomes so small that viscosity damps the waves and restores waveless motion. In practical applications, it is the first of these situations that is used.

To illustrate key features of the SDA process, we consider as our base case atomization of a 40% glycerol-water mixture with the following characteristics: $\rho = 1.11$ g cm^{-3}, $\mu = 5.3$ mPa s, $\sigma = 74.3$ mN m^{-1}, $R_d = 2.5$ cm, $Q = 8$ ml s^{-1}, $\Omega = 220$ rad s^{-1}, and $z_{cl} = 1$ mm. These parameters are in the range which, according to experiments,[3,5,6] corresponds to a fully developed ligament regime. This base case also allows us to compare the volumes of the resulting drop with those observed in experiments of Wang *et al.*[6]

For the above parameters, one has $n_{\mathrm{jet}} = 79$ and the following scales for length and velocity: $H = 5.84 \times 10^{-3}$ cm, $U = 9.44 \times 10^2$ cm s^{-1}. The corresponding similarity parameters are Re = 116, We = 78, Fr = 395, Rb = 733, $R_d^* = 428$, and $z_{cl}^* = 17$.

Note that variation of the operational parameters can cause step-changes in the number of jets and hence in the scales, notably in the size of the computational domain in the azimuthal direction. Computationally, this is inconvenient so that, to avoid problems with convergence, the computational domain in the transition zone is rescaled using fixed length and velocity scales.

1. Azimuthal drifting of the jet as a whole

The first qualitative feature that should be noted is that, even for a waveless flow, there is a distinct azimuthal drift of the jet as a whole with respect to the disk, i.e., $\Delta\Omega = \Omega - \Omega_j \neq 0$. The jet lags behind the rotating disk; this lag depends on the flow conditions, and, as one can see in Fig. 4 (left), the relative azimuthal drift, $\Delta\Omega/\Omega$, increases with the flow rate Q and decreases with the increase in the angular velocity of the disk. The dependence of $\Delta\Omega/\Omega$ on the flow rate is easy to understand. At a fixed angular velocity, an increase in the flow rate leads to a rise of the flow velocity in the radial direction and hence the Coriolis force responsible for the drift also increases. The role of the angular velocity is less obvious as the Coriolis

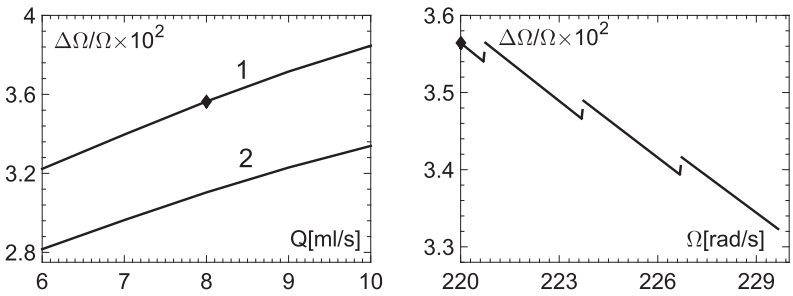

FIG. 4. The dependence of the relative azimuthal drifting speed of the jet $\Delta\Omega/\Omega = (\Omega - \Omega_j)/\Omega$ on the flow rate Q for different angular velocities of the disk (left), where curves 1 and 2 correspond to $\Omega = 220$ rad s^{-1} and 240 rad s^{-1}, respectively, and on the angular velocity (right). The step-changes in the plot correspond to the changes in the number of outgoing jets, increasing from left to right: $n_{\text{jet}} = 79$, 80, 81, and 82. In both plots, the black marker corresponds to the base case.

force increases with Ω both directly and indirectly (due to an increase in the radial velocity of the flow resulting from an increase in the centrifugal force that drives the flow). However, this increment in the absolute drift $\Delta\Omega$ is smaller than the corresponding increase in Ω itself so that the relative azimuthal drift $\Delta\Omega/\Omega = 1 - \Omega_j/\Omega$ goes down.

The dependence of $\Delta\Omega/\Omega$ on Ω is complicated even further, see Fig. 4 (right), since an increment in Ω changes the number of jets n_{jet} determined by (26) and (27) and this has the corresponding effect on the relative azimuthal drift of the jets.

Although the azimuthal drift of the jets with respect to the disk is a small effect, it has serious implications. First, since we are interested in a regular regime of the drop generation, not a flow picture shortly after the start of the computations, it is necessary to take the relative drift of the jet into account as otherwise the flow domain becomes distorted shortly after the computations begin: the jet moves to one side of the flow domain squashing the mesh there and ultimately making further computation impossible.

The azimuthal drift of the jets also has practical implications as it suggests that a disk with boundaries preventing the jets from drifting with respect to the disk would influence the flow field near the disk's edge making it different from that observed for an unstructured smooth disk. In particular, the potential effect of the disk profiling on the number of jets is bound to affect the size of the drops produced as the result of the SDA process.

2. *Flow field and the free surface profile*

Figure 5 shows a typical flow field in the part of the transition zone around the disk's edge. The top view (Fig. 5, left) gives the velocity on the free surface, i.e., as it can be directly observed experimentally. The side view (Fig. 5, right) shows the velocity distribution in the cross section of the flow domain by a vertical surface going, first, along the radius and, after reaching the disk's edge, along the jet's centerline.

In the top view of the flow field (Fig. 5, left), the very left arrow pointing toward the boundary shows that there is a bit of swirling of the flow which soon dies out. Importantly, all traces of three-dimensionality of the flow vanish within a few diameters of the jet and further down one has a uniform flow, which justifies the use of Euler's equations for a part of the jet's "stem" in the transition zone and for the region.

As one can see in the side view (Fig. 5, right), the fluid goes over the disk's upper edge and leaves the disk close to its bottom edge. This might seem a bit counterintuitive as, for the angular velocities of hundreds rad/s, one would expect the film to "fly off" the disk's surface. However, this does not happen as the film is simply too thin, and near the disk's edge the capillary pressure of the (curved) free surface can withstand the fluid's inertia and re-direct the film along the disk's side. The case of an ultra-thin disk, where its thickness is comparable or less than the thickness of the film has not been explored and, perhaps, deserves attention in the future.

Notably, though the influence of gravity for the base case shown in the figure is negligible, the asymmetry of the flow configuration with respect to any horizontal plane results in the departing jet's being not horizontal, i.e., having a downward component of velocity. This reinforces the point made in Ref. 37 that the situation often considered in theoretical studies on the spiralling jets atomizers, where it is assumed that the jet trajectories lie in a horizontal plane, is not what is to be expected in applications.

The bottom edge of the disk plays an important role: after the fluid turns round the top edge of the disk, essentially it is the contact line pinned to the bottom edge that prevents it from going further down so that the fluid has to form a jet and leave the disk. This is illustrated in Fig. 6, which shows the free-surface profile in the vertical cross section (again, going along

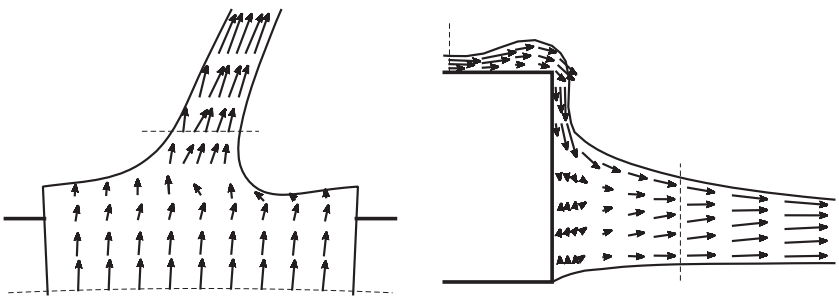

FIG. 5. The velocity field near the disk's edge. Left: the top view showing the velocity as it is seen on the free surface. Right: the side view showing the velocity in the vertical cross section by a surface that goes, first, along the disk's radius and then, on reaching the disk's edge, along the jet's centerline. The disk's boundary is shown as a thicker line in both plots. The flow parameters correspond to the base case.

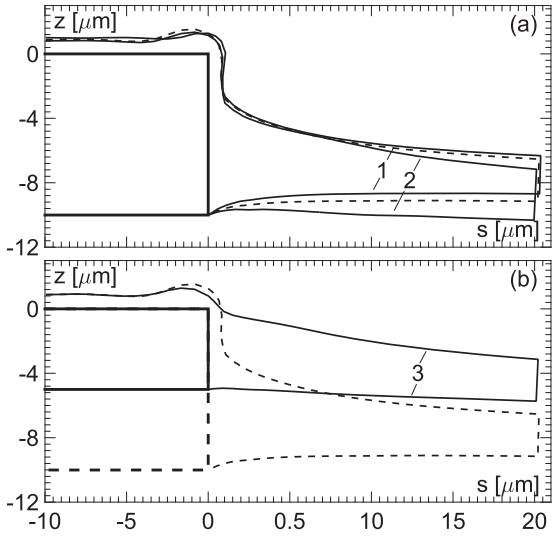

FIG. 6. The free surface profile in the vertical cross section. In both figures, the dashed line corresponds to the base case. The variations from the base case are as follows: (1) $\Omega = 240$ rad s^{-1}; (2) $Q = 10$ ml s^{-1}; (3) $z_{cl} = 0.5$ mm.

the radius on the disk and along the jet's centerline beyond the disk's rim). The free surface profile varies in response to the variation of the angular velocity, the flow rate, and the position of the contact line. In the range of parameters considered, the influence of the first two factors appears to be relatively small whilst the position of the contact line has a very significant effect. Essentially, it is the location of the contact line that determines the vertical position of the jet leaving the disk.

3. Contact angle variation

The role of the location of the contact line is illustrated in Fig. 7, where we show the azimuthal distribution of the contact angle formed by the free surface with the lateral (vertical) side of the disk (Fig. 1) for the same parameters as in Fig. 6. The contact angle reaches its maximum near the place where the jet leaves the disk and a minimum close to it. In the situation where the contact line goes along the bottom edge of the disk, it cannot advance but can recede if the contact angle drops

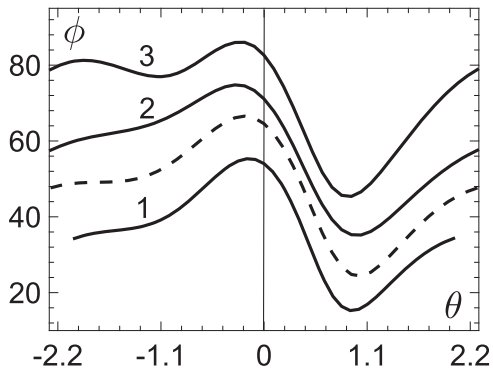

FIG. 7. The dependence of the contact angle ϕ formed by the free surface and the side wall of the disk on the azimuthal (polar) angle θ in the plane of the disk parameterizing the disk's rim in the representative sector. The jet's centerline corresponds to $\theta = 0$. The base case is shown as the dashed line, and curves 1, 2, and 3, as in Fig. 6, correspond to $\Omega = 240$ rad s^{-1}, $Q = 10$ ml s^{-1}, and $z_{cl} = 0.5$ mm, respectively.

below the static receding angle bounding the contact angle hysteresis.[77] The latter combined with the azimuthal drift of the jet means that, even for the waveless flow in the film, one has the moving contact line on the disk's lateral side. This will significantly change the flow field in the transition zone and, as far as the simulation is concerned, brings in the moving contact-line problem. Besides the difficulties associated with the modeling side (see Ref. 49 for a review), this involves a huge computational cost since, as shown in Refs. 53 and 69, the accurate simulation of the contact-line motion requires a very high spatial resolution (spanning several orders of magnitude in terms of the mesh size) near the contact line to resolve all the scales involved.

In this regard, thin disks have an advantage but, at the same time, if the disk is "too thin," then, as indicated by the variation of z_{cl} (curve 3, Fig. 7), the contact angle can go over 90° and the contact line would be able to advance across the bottom side of the disk. In practical terms, this would mean erratic irregular atomization. Thus, even on a qualitative level, one can say that there exists an optimal thickness of the disk, or perhaps a range, which ensures pinning of the contact line, and the simulation of the flow in the transition zone alone allows one to determine it.

4. Drop formation

A few jet diameters from the jet's starting point, the jet becomes convectively unstable to disturbances coming from the spinning disk vibrations and picks the fastest spatially growing wave there which then propagates down the jet as described in Ref. 40. The centrifugal force stretches the jet making the base flow spatially vary so that, in the linear regime, both the amplitude and the wavelength of this wave increase. Further down the jet, the wave's evolution becomes nonlinear and, shortly after entering the nonlinear regime, the nonlinear dynamics results in the formation of a drop which then breaks away from the jet's end. The distance ξ_b from the starting point of the jet to the point where the drop breaks away depends on the amplitude of the disturbances at the onset of convective instability. A study of the role played by the amplitude and frequency of inlet perturbations for straight jets can be found in Ref. 78. In practice, the amplitude of initial disturbances is not known, so that, qualitatively referring to these disturbances as the trigger of the instability, quantitatively it is more convenient to inverse the problem and characterize them by ξ_b. Then smaller values of ξ_b correspond to stronger initial disturbances and vice versa. For simplicity, in practice, one can neglect the distance between the disk and the "starting point of the jet" (Fig. 1) and associated ξ_b with the easily measurable distance from the disk to the breakup point.

The drop formation can follow different scenarios depending on the magnitude of the disturbances coming from the disk vibration and corresponding to different values of ξ_b. These scenarios, which are illustrated in Fig. 8 and summarized in Fig. 9, can be described as follows. For large amplitudes of the disturbances at the onset of convective instability, the fastest spatially growing wave enters the nonlinear regime of its evolution close to the point where it was initiated so that its wavelength, which increases as the wave propagates down the stretching jet, does not have the room to increase much

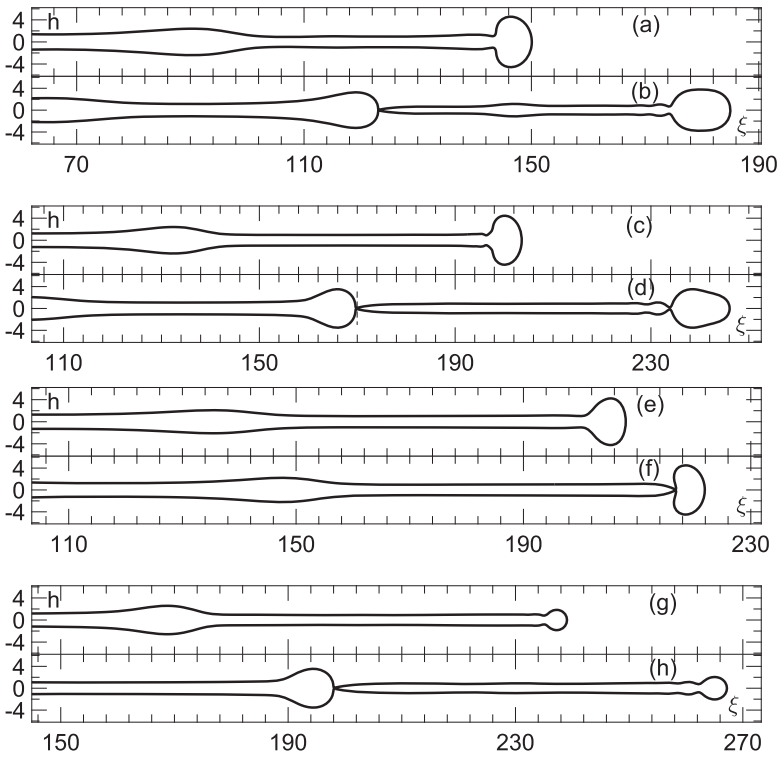

FIG. 8. Typical free-surface profiles for three different scenarios of the jet breakup corresponding to different amplitudes of the incident wave. Frames (a) and (b): "large" amplitude leading to the satellite-free regime; the drop detaches close to the starting point of the jet; (c) and (d): "medium" amplitude leading to the (almost) simultaneous detachment of the main drop and the satellite droplet; the detachment of the drop/satellite happens further away from the starting point of the jet; (e)–(h): "small" amplitude of the incident wave resulting in the primary drop [(e) and (f)] followed by a satellite [(g) and (h)]; the distance to the point where the main drop and the satellite detach increases as the amplitude of the incident disturbance goes down. The terms "large," "medium," and "small" referring to the amplitude are used descriptively as all regimes correspond to the incident wave beginning its propagation in the linear regime. Both lengths on the axes are scaled with H defined in (28).

when this wave leads to the capillary breakup and the departure of a newly formed drop. This situation is illustrated in Figs. 8(a) and 8(b). The next drop will be formed in the same way with no satellite droplets in between. It should be noted here that the detached drop may or may not itself break up after it detaches from the jet or the drops that are produced may or may not coalesce back into larger ones; here, we are considering only the primary breakup without following the subsequent evolution of the drops that are produced. Hence the terms "single drop" and "satellite-free regime" refer only to the primary breakup.

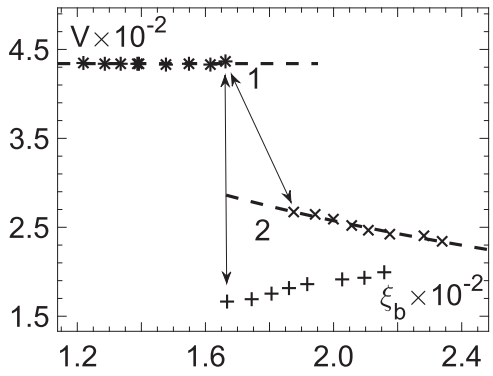

FIG. 9. Dependence of the volume of the drops/satellites, V, on the distance from the starting point of the jet to the pinch-off point, ξ_b, for the flow parameters of the base case. ✳: the drop in the satellite-free regime; ×: the main drop; +: the satellite. The arrows indicate the transition regime where the primary breakup can occur in either of the two necks connecting the detaching part of the jet from the rest of it. Dashed line 1 is $V = 434.1$; dashed line 2 approximates the volumes of the main drop as $V(\xi_b) = C_1 h_0(\xi_b) + C_2$, where h_0 is the radius of the unperturbed jet, $C_1 = 484.6$, and $C_2 = -380.5$. The distance ξ_b and the volume V are scaled with H and H^3, respectively, where H is defined in (28).

In Fig. 9, we show the volume of the drops produced (scaled with H^3) versus the distance ξ_b from the starting point of the jet to the breakup point, and the above "single drop" scenario is marked by the "snowflake" (✳). For strong initial disturbances, the "snowflake" is close to the vertical axis, i.e., the pinch-off happens close to the disk. For weaker initial disturbances, the corresponding "snowflake" moves further away from the vertical axis as the drop pinches off at larger distances from the disk whilst the volume of the resulting single drop remains constant. This continues until the drop formation process enters a transition/irregular regime illustrated in Figs. 8(c) and 8(d). In this regime, the neck connecting the forming main drop with the future satellite droplet and the neck connecting this future satellite droplet with the next main drop vanish (almost) simultaneously. Then, one can have either a single drop (made up of the main drop and the satellite droplet) detaching closer to the disk (and breaking up immediately afterwards) or the main drop detaching first further away from the disk and almost immediately followed by a satellite droplet detaching closer to the disk. In the next cycle, the process repeats. In Fig. 9, this transition scenario is indicated by the arrows showing the correspondence of the single drop and the main drop-satellite droplet pair. (The essence of the process is emphasized by our choice of symbols as ✳ corresponding to a single drop is made of × marking the main drop and + refers to the satellite.)

Finally, if the amplitude of the initial disturbances is reduced further, the wavelength of the fastest spatially growing wave as it enters the nonlinear regime is already so large that the drop formation regime becomes regular again, with the main drop detaching before a satellite is formed, as shown in Figs. 8(e) and 8(f), followed by the formation and detachment of the satellite droplet [Figs. 8(g) and 8(h)]. In Fig. 9, this

regime corresponds to the main drops (×) and satellite droplets (+) whose volumes gradually converge and the detachment points get further away from the disk as the amplitude of the incident disturbances decreases. It is noteworthy that as Ω is reduced, the single-drop (satellite-free) region shrinks until it vanishes completely so that for angular velocities below a certain value, one has no satellite-free scenario and the main drop is always followed by a satellite droplet. As found in Ref. 40, the volume of the main drop in this regime is a linear function of the radius h_0 of the unperturbed jet evaluated at the detachment point,

$$V(\xi_b) = C_1 h_0(\xi_b) + C_2. \tag{38}$$

The values of constants C_1 and C_2 are given in the caption of Fig. 9. This equation relating the volume of the main drop with the easy-to-calculate unperturbed radius of the jet h_0 can be used in experiments as a guide indicating the strength of disturbances present in the system.

5. Comparison with experimental data

Experimental papers normally report one single drop size as the outcome of the SDA process and, unsurprisingly, give no information regarding the magnitude of the parasitic vibrations coming from the atomizer that trigger convective instability in the outgoing jets. It is this single size that becomes the basis of different empirical correlations, e.g., Ref. 3.

In Fig. 10, we compare our simulation results for the 40% glycerol-water mixture with the experimental data reported recently in Ref. 6. Open squares with error bars show the experimentally measured diameters of the equivalent spherical drops for different angular velocities of the disk taken from Fig. 12(a) of Ref. 6 whilst the symbol ✳, as before, refers to the single drop in the satellite-free regime and the symbols ×, + correspond to the main drop and the satellite droplet in the regime where satellites are present and, as previously discussed, the latter cover a range of drop sizes depending on the magnitude of the initial disturbances responsible for the instability in the jet. The dashed line in Fig. 10 shows the empirical correlation suggested by Frost.[3]

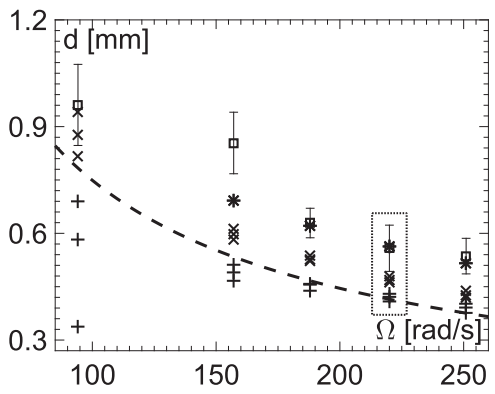

FIG. 10. Comparison of the simulation results (✳, ×, and + as in Fig. 9) with experimental data (squares with error bars) reported in Fig. 12(a) of Ref. 6. The diameter, d, on the vertical axis is that of an equivalent spherical drop. The dashed line shows the empirical relationship proposed by Frost.[3] The data at Ω = 220 rad/s (in the box) correspond to the base case; see Fig. 9. At Ω = 94 rad/s, there is no satellite-free regime in our calculations.

As one can see, the simulation results come much closer to the experimental data reported by Wang *et al.*[6] than the empirical relationship,[3] especially at higher angular velocities where the agreement is excellent. Notably, one can expect a higher level of parasitic vibrations/noise in the atomizer at higher angular velocities of the disk rotation and hence expect that the drop formation would take place in the satellite-free regime so that it should be the single drop size (✳) that would be closest to the experimental data. As one can see in Fig. 10, this is indeed the case. Thus, we can conclude that the comparison with experimental data supports our conjecture regarding the origin of the disturbances that determine the drop formation process. As mentioned earlier, the single-drop regime shrinks as the angular velocity of rotation decreases, and, as we can see in Fig. 10, at the lowest angular velocity, it is the size of the main drop (followed by a satellite droplet) which has been measured whilst at higher velocities it was the single drop.

B. Atomization from a wavy film

Another case with reproducible atomization is where the disk is sufficiently large so that an externally imposed frequency can synchronize the waves and the size of the disk allows the dominating wave to fully develop. Then, the dominating wave in the film is converted by the transition zone into long waves in the outgoing jets and these waves modulate the size distribution of the drops whilst the drops themselves, as before, result from the high-frequency disturbances coming from the atomizer.

To illustrate the main features of the SDA process in this regime, we use as our new base case the following set of dimensional parameters: $\rho = 1$ g/cm^3, $\mu = 0.1$ mPa s, $\sigma = 50$ mN/m, $R_d = 6$ cm, $z_{\rm cl} = 0.2$ cm, $Q = 20$ ml/s, and $\Omega = 50$ rad/s so that $H = 0.0152$ cm and $U = 3.61$ m/s and consequently Re = 55, We = 40, Rb = 474, Fr = 93, $n_{jet} = 76$, $R_d^* = 393.81$, and $z_{cl}^* = 13.13$. At the location of S_1, we have $\delta = 0.19$ and E = 6.86.

1. Wavy drifting and conversion of disturbances by the transition zone

Once the external frequency is imposed, the flow acquires a host of new features. First, the waves generated in the film region cause variations in the flow rate thus making the jet as a whole not only wobble, both vertically and horizontally, but also on average drift azimuthally at a speed that differs from the speed in the waveless regime. This is one of the manifestations of nonlinearity of the system as time-periodic deviations of the flow rate above and below its average value make different contributions to the drifting speed. Figure 11 shows how the jet as a whole drifts once the (dimensionless) frequency $\omega^* = 9.4 \times 10^{-2}$ is imposed on the base case flow. The unsteady drifting of the jet as a whole has serious implications for the simulations. Whilst for the flow in the transition zone it is convenient to keep the baseline of the mesh steady with the flow variation accounted for by the unsteady finite-element code, for the jet, computationally, it becomes necessary to consider the jet in the coordinate frame moving with its centerline and hence introduce unsteadiness elsewhere.

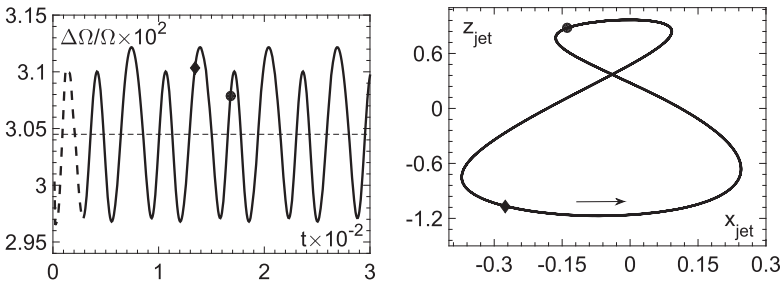

FIG. 11. Left: variation of the relative drifting speed of the jet as a function of time; right: the trajectory of the jet's centerline in the plane normal to it for $\omega^* = 9.4 \times 10^{-2}$. The dashed line (left plot) shows the calculations before the regular (periodic) regime is reached; the horizontal (thin) dashed line indicates the time-averaged value of $\Delta\Omega/\Omega$. The two markers show the correspondence between the left and the right plots.

The central issue in the SDA process from a wavy film is how the waves in the film are converted into disturbances in the outgoing jets as the waves go through the transition zone. In this regard, one should have in mind that there are many types of waves that are possible in the film, so here we will consider as an example only one wave family.

Figure 12 shows the "raw data," i.e., the time-dependence of the thickness of the film at S_1 and the radius of the jet at S_2 with the corresponding variation of the velocity on the free surface. One can see that the oscillations of the film thickness are significantly amplified as they are passed on to the jet and the process looks periodic. This periodicity is confirmed once we consider the phase diagram shown in Fig. 13 which is obtained by eliminating the time from Fig. 12. As Fig. 13 shows, once the influence of the initial conditions imposed to start the computations dies out, in the jet radius versus the film thickness plane and in the corresponding velocity plane, the system follows a closed path which, for the family of waves in the film corresponding to the parameters of our base case, have a very simple form. These closed paths play the role of an integral "signature" of the transition zone summarizing the effect of the essentially 3D unsteady motion. Computations show that the shape of the phase diagrams varies insignificantly with variations of the flow rate and the speed of rotation. Reproducibility of the phase diagrams after many waves pass through the transition zone can also be used as a check on the accuracy and robustness of the computations.

2. Drop formation

A nonlinear dominating wave in the film on the disk modulates the flow rate in the outgoing jets so that the onset of convective instability, its development along the jet, and the eventual formation of drops at the jet's end takes place at different times essentially for different jets. Figure 14 (left) shows how the variation of the flow rate in the film at S_1 is converted, with a certain time-lag, into the variation of the flow rate at S_2, i.e., in the outgoing jet. The development of convective instability occurs on a much shorter time scale so that for the flow rates marked with open circles one has different ranges of drop sizes, Fig. 14 (right). As reported in Ref. 40, the time period for producing a single drop in the satellite-free regime and a main drop plus a satellite droplet in the regime corresponding to weaker incident is the same for a given flow rate, though the share of this period going into the production of the main and the satellite droplet depends on how far down the jet they are produced, i.e., on the amplitude of the disturbances at the onset of convective instability. These periods (in the dimensionless units) for the five groups of data shown in Fig. 14 (right) are (from left to right) $T = 0.66$, 0.80, 1.09, 1.34, and 1.45. Using this information, one can, if necessary, evaluate the

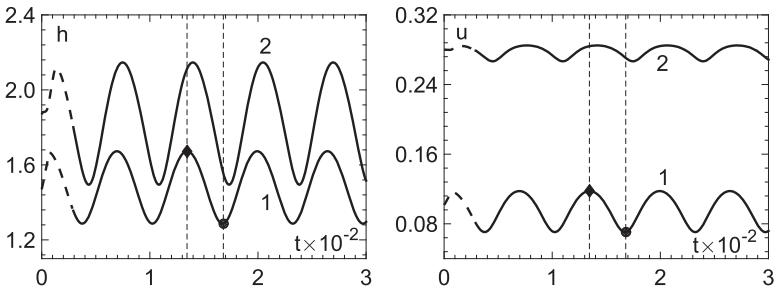

FIG. 12. Left: the film thickness at S_1 (curve 1) and the jet radius at S_2 (curve 2) as functions of time. Right: the corresponding time-dependence of the velocity on the free surface. The dashed line shows the beginning of the computations. The markers show the corresponding points. $\omega^* = 9.4 \times 10^{-2}$; the flow parameters correspond to the base case.

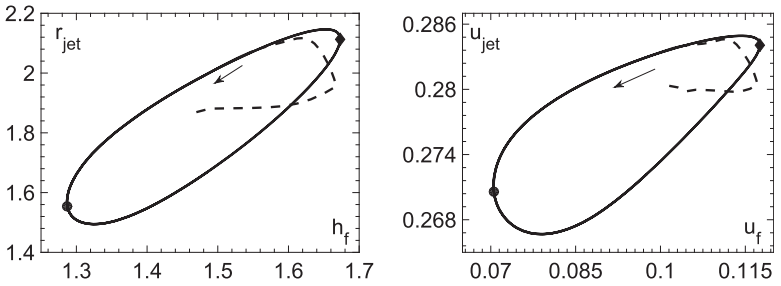

FIG. 13. The phase diagrams corresponding to Fig. 12 with the time eliminated: the dependence of the jet radius at S_2 from the film thickness at S_1 (left) and the corresponding plot for the velocities. The marker shows the correspondence between the plots and the arrow indicates the direction of variation as t increases. The dashed line shows the beginning of the computations.

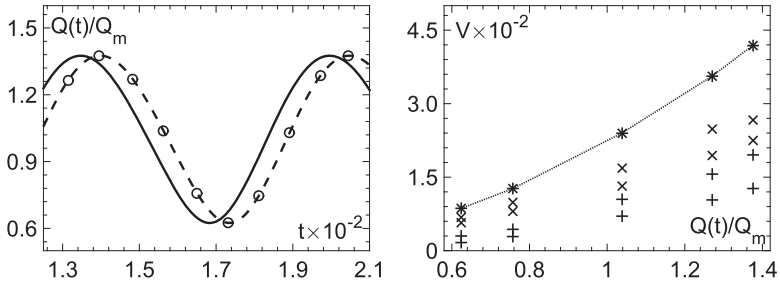

FIG. 14. The modulation of the drop size by the waves in the film on the disk. Left: the time-dependence of the flow rate at the inlet S_1 of the transition zone (solid line) and at the outlet S_2 (dashed line). Right: the range of the drop volumes corresponding to different flow rates. Symbols ✳, ×, and + correspond to the only drop, the main drop, and the satellite droplet, respectively. The time-dependent flow rate $Q(t)$ is normalized by its mean value Q_m. The nine markers (open circles) within one period of oscillations in the left plot spaced by equal time intervals collapse into 5 groups of the data in the right plot as the same flow rates correspond to the same range of drops produced. The dotted line connecting the largest volume of drops is there to show the trend.

distribution of the drop volumes corresponding to one period of the wave in the film.

Note that for the atomization in the wavy regime, the disparity of the time scales characterizing the waves in the film on the disk and characterizing the drop formation process invariably leads to a range of drop sizes, even for the single-drop regime. This conclusion differs qualitatively from the outcome of Ref. 73 where the simulations based on a commercial software package predicted uniform drops for the wavy ("turbulent") regime of the film flow with a completely different mechanism of drop formation and the drop size on the scale of the jet's diameter.

VII. SUMMARY

In Secs. III–V, we describe the method developed for the simulation of the spinning disk atomization process as a whole, from the film flow on the rotating disk to the formation and detachment of drops at the ends of the liquid jets that spiral away from the disk's rim. A head-on computational simulation of the whole process is beyond available computational resources as, on the one hand, the flow involves disparate characteristic length and time scales and, on the other, requires high accuracy in handling its main elements. The adopted approach is based on splitting the flow into elements, utilizing, where possible, known asymptotic simplifications, and putting them together in the way which preserves the exchange of information between them. The main elements of the spinning disk atomization flow are: (i) the film flow over the rotating disk, (ii) the flow in the transition zone near the disk's rim where the film breaks into separate jets, (iii) the dynamics of a spiral jet, and (iv) the capillary breakup of the jet.

The film flow in the waveless regime for small disks is described by simple analytic formulas (9)–(12). For larger disks, one has to take into account the nonlinear waves resulting from the instability of the waveless flow. The corresponding formulas (14)–(16) involve the solution of an eigenvalue problem which is rather intricate. One can address this problem and efficiently explore the parameter space, which is necessary to find the dominating wave, using the invariant embedding method[35] though this still remains a rather challenging and laborious task.

For the dynamics of spiral jets, there is a relatively simple mathematical framework,[37] and, once the parameters of a jet are found, the propagation of disturbances along it can be described in a straightforward way.[40] The problem is, first, to determine where the separate free-surface streams into which the film disintegrates as it leaves the disk become "jets" and hence the mathematics developed for the jets becomes applicable. Given that the future jet starts from a wide base on the disk and a near-zero velocity, the second issue is to determine the flow characteristics of the outgoing jet. Finally, once we have a "jet" and its characteristics, we have to determine the wavelength of the disturbances which will eventually create the drops. The first two of these issues have been addressed by simulating the free-boundary flow in the transition zone near the disk's rim by determining the position and orientation of the outlet cross section S_2 and matching the flow there with that of the jet. Then, once the parameters of the jet have been obtained, one can follow the jet's trajectory backwards to determine where it starts and hence obtain the "starting point of the jet" (Fig. 1) from which the mathematical framework of Ref. 37 becomes applicable.

In determining the origin of the disturbances that lead to the drop formation, we had to conclude that it is not the background noise everywhere along the jet as this would lead to the drops with the sizes determined by the local Rayleigh instability and, as an analysis of experiments shows, these are much smaller than the sizes of the drops observed experimentally. The physical conjecture prompted by experiments[75,76] and used in this work is that the noise comes from the atomizer, i.e., from the mechanics of the rotating disk. Then, as the jet begins to develop, it becomes convectively unstable. It is conjectured that it is the spatially fastest growing mode picked at the onset of convective instability that is the one that develops into a nonlinear wave which eventually leads to the capillary breakup of the jet. The comparison of the simulation results with the experimental data of Ref. 6 supports this conjecture.

A useful indicator for experimental work is Eq. (38) for the volume of the main drop as a function of the easy-to-calculate radius h_0 of the unperturbed jet. This fitting equation, found in Ref. 40 and confirmed here, together with the wavelength at the onset of convective instability, which determines the size of the drop in the satellite-free scenario, essentially gives one a guide to the primary capillary breakup in the spinning disk atomization process and, in particular, makes it possible to assess the level of parasitic noise coming from the atomizer.

The feature of the spinning disk atomization flow which remains an outstanding issue for the modeling is the number of jets that are produced from a film of a given fluid under given flow conditions. In the present study, we used an empirical formula from an experimental paper by Frost,[3] and, although for practical purposes Frost's formula is entirely adequate, further research is required if the number of jets is to be predicted theoretically. Existing approaches to this problem, e.g., Refs. 79 and 80, have been only partially successful.

ACKNOWLEDGMENTS

This work was supported by the Engineering and Physical Sciences Research Council (UK) under Grant No. EP/K028553/1 and in part by the Russian Foundation for Basic Research in the framework of Project No. 17–01–00057.

[1] A. J. Hewitt, "Droplet size spectra produced by the X15 stacked spinning-disk atomizer of the Ulvamast Mark II sprayer," Crop Prot. **11**, 221–224 (1992).
[2] A. J. Hewitt, "Droplet size spectra produced by air-assisted atomizers," J. Aerosol Sci. **24**, 155–162 (1993).
[3] A. R. Frost, "Rotary atomization in the ligament formation mode," J. Agric. Eng. Res. **26**, 63–78 (1981).
[4] L. Qi, P. C. H. Miller, and Z. Fu, "The classification of the drift risk of sprays produced by spinning discs based on wind tunnel measurements," Biosyst. Eng. **100**, 38–43 (2008).
[5] H. Peng, N. Wang, D. Wang, and X. Long, "Experimental study on the critical characteristics of liquid atomization by a spinning disk," Ind. Eng. Chem. Res. **55**, 6175–6185 (2016).
[6] D. Wang, X. Ling, H. Peng, Z. Cui, and X. Yang, "Experimental investigation of ligament formation dynamics of thin viscous liquid film at spinning disk edge," Ind. Eng. Chem. Res. **55**, 9267–9275 (2016).
[7] X. Li and M. C. Soteriou, "High fidelity simulation and analysis of liquid jet atomization in a gaseous crossflow at intermediate Weber numbers," Phys. Fluids **28**, 082101 (2016).
[8] X. Li, H. Gao, and M. C. Soteriou, "Investigation of the impact of high liquid viscosity on jet atomization in crossflow via high-fidelity simulations," Phys. Fluids **29**, 082103 (2017).
[9] J. X. Liu, Q. B. Yu, and Q. Guo, "Experimental investigation of liquid disintegration by rotary cups," Chem. Eng. Sci. **73**, 44–50 (2012).
[10] B. Ambravaneswaran, H. J. Subramani, S. D. Phillips, and O. A. Basaran, "Dripping-jetting transitions in a dripping faucet," Phys. Rev. Lett. **83**, 034501 (2004).
[11] A. Lawley, *Atomisation: Production of Metal Powders* (Metal Powder Industries Federation, Princeton, New Jersey, 1992).
[12] N. C. Jacobsen and O. Hinrichsen, "Micromixing efficiency of a spinning disk reactor," Ind. Eng. Chem. Res. **51**, 11643–11652 (2012).
[13] Y. Senuma, S. Franceschin, J. G. Hilborn, P. Tissières, I. Bisson, and P. Frey, "Bioresorbable microspheres by spinning disk atomization as injectable cell carrier: From preparation to *in vitro* evaluation," Biomaterials **21**, 1135–1144 (2000).
[14] M. Ahmed and M. S. Youssef, "Characteristics of mean droplet size produced by spinning disk atomizers," J. Fluids Eng. **134**, 071103 (2012).
[15] P. Sungkhaphaitoon, S. Wisutmethangoon, and T. Plookphol, "Influence of process parameters on zinc powder produced by centrifugal atomisation," Mater. Res. **20**, 718–724 (2017).
[16] G. Charalampous and Y. Hardalupas, "How do liquid fuel physical properties affect liquid jet development in atomisers?," Phys. Fluids **28**, 102106 (2016).
[17] M. Akhtar, B. S. Murray, E. I. Afeisume, and S. H. Khew, "Encapsulation of flavonoid in multiple emulsion using spinning disc reactor technology," Food Hydrocolloids **34**, 62–67 (2013).
[18] K. V. K. Boodhoo and R. J. Jachuck, "Process intensification: Spinning disc reactor for condensation polymerisation," Green Chem. **2**, 235–244 (2000).
[19] P. Oxley, C. Brechtelsbauer, F. Ricard, N. Lewis, and C. Ramshaw, "Evaluation of spinning disk reactor technology for the manufacture of pharmaceuticals," Ind. Eng. Chem. Res. **39**, 2175–2182 (2000).
[20] S. D. Pask, O. Nuyken, and Z. Cai, "The spinning disk reactor: An example of a process intensification technology for polymers and particles," Polym. Chem. **3**, 2698–2707 (2012).
[21] K. Norrman, A. Ghanbari-Siahkali, and N. B. Larsen, "Studies of spin-coated polymer films," Annu. Rep. Prog. Sect. C: Phys. Chem. **101**, 174–201 (2005).
[22] S. Sahoo, A. Arora, and P. Doshi, "Two-layer spinning flow of Newtonian liquids: A computational study," Comput. Fluids **131**, 180–189 (2016).
[23] S. Sahoo, A. V. Orpe, and P. Doshi, "Spreading dynamics of superposed liquid drops on a spinning disk," Phys. Fluids **30**, 012110 (2018).
[24] O. K. Matar, G. M. Sisoev, and C. J. Lawrence, "The flow of thin liquid films over spinning discs," Can. J. Chem. Eng. **84**, 625–642 (2006).
[25] H. Espig and R. Hoyle, "Waves in a thin liquid layer on a rotating disk," J. Fluid Mech. **22**, 671–677 (1965).
[26] A. F. Charwat, R. E. Kelly, and C. Gazley, "The flow and stability of thin liquid films on a rotating disk," J. Fluid Mech. **53**, 227–255 (1972).
[27] W. P. Woods, "The hydrodynamics of thin liquid films flowing over a rotating disc," Ph.D. thesis, University of Newcastle, Newcastle upon Tyne, UK, 1995.
[28] A. I. Butuzov and I. I. Puhovoi, "Liquid-film flow regimes on a rotating surface," J. Eng. Phys. **31**, 886 (1976).
[29] S. Thomas, A. Faghri, and W. Hankey, "Experimental analysis and flow visualization of a thin liquid film on a stationary and rotating disk," J. Fluids Eng. **113**, 73–80 (1991).
[30] P. L. Kapitza and S. P. Kapitza, "Wave flow of thin viscous liquid films. III. Experimental study of wave regime of a flow," J. Exp. Theor. Phys. **19**, 105–120 (1949).
[31] S. V. Alekseenko, V. E. Nakoryakov, and B. T. Pokusaev, in *Wave Flow of Liquid Films* (Begell House, Inc., NY, 1994), p. 313
[32] J. Liu and J. P. Gollub, "Onset of spatially chaotic waves on flowing films," Phys. Rev. Lett. **70**, 2289–2292 (1993).
[33] J. Liu, J. D. Paul, and J. P. Gollub, "Measurements of the primary instabilities of film flows," J. Fluid Mech. **250**, 69–101 (1993).
[34] J. Liu and J. P. Gollub, "Solitary wave dynamics of film flows," Phys. Fluids **6**, 1702–1712 (1994).
[35] G. M. Sisoev, O. K. Matar, and C. J. Lawrence, "Axisymmetric wave regimes in viscous liquid film flow over a spinning disk," J. Fluid Mech. **495**, 385–411 (2003).
[36] V. M. Entov and A. L. Yarin, "The dynamics of thin liquid jets in air," J. Fluid Mech. **140**, 91–111 (1984).
[37] Y. D. Shikhmurzaev and G. M. Sisoev, "Spiralling liquid jets: Verifiable mathematical framework, trajectories and peristaltic waves," J. Fluid Mech. **819**, 352–400 (2017).
[38] P. Huerre and P. A. Monkewitz, "Local and global instabilities in spatially developing flows," Annu. Rev. Fluid Mech. **22**, 473–537 (1990).
[39] S. Le Dizès and E. Villermaux, "Capillary jet breakup by noise amplification," J. Fluid Mech. **810**, 281–306 (2017).
[40] Y. Li, G. M. Sisoev, and Y. D. Shikhmurzaev, "On the breakup of spiralling liquid jets," J. Fluid Mech. (in press).
[41] Y. D. Shikhmurzaev, "Capillary breakup of liquid threads: A singularity-free solution," IMA J. Appl. Math. **70**, 880–907 (2005).
[42] J. R. Castrejón-Pita, A. A. Castrejón-Pita, S. S. Thete, K. Sambath, I. M. Hutchings, J. Hinch, J. R. Lister, and O. A. Basaran, "Plethora of transitions during breakup of liquid filaments," Proc. Natl. Acad. Sci. U. S. A. **112**, 4582–4587 (2015).
[43] Y. Li and J. E. Sprittles, "Capillary breakup of a liquid bridge: Identifying regimes and transitions," J. Fluid Mech. **797**, 29–59 (2016).
[44] Y. D. Shikhmurzaev, "Macroscopic mechanism of rupture of free liquid films," C. R. Mec. **333**, 205–210 (2005).
[45] M. Bowen and B. S. Tilley, "On self-similar thermal rupture of thin liquid sheets," Phys. Fluids **25**, 102105 (2013).
[46] J. E. Sprittles and Y. D. Shikhmurzaev, "Coalescence of liquid drops: Different models versus experiment," Phys. Fluids **24**, 122105 (2012).
[47] J. E. Sprittles and Y. D. Shikhmurzaev, "The coalescence of liquid drops in a viscous fluid: Interface formation model," J. Fluid Mech. **751**, 480–499 (2014).
[48] J. E. Sprittles and Y. D. Shikhmurzaev, "Dynamics of liquid drops coalescing in the inertial regime," Phys. Rev. E **89**, 063008 (2014).
[49] Y. D. Shikhmurzaev, *Capillary Flows with Forming Interfaces* (Chapman & Hall/CRC, Boca Raton, Toronto, New York, 2007).
[50] G. M. Sisoev, D. B. Goldgof, and V. N. Korzhova, "Stationary spiral waves in film flow over a spinning disk," Phys. Fluids **22**, 052106 (2010).

[51]T. D. Blake, M. Bracke, and Y. D. Shikhmurzaev, "Experimental evidence of nonlocal hydrodynamic influence on the dynamic contact angle," Phys. Fluids **11**, 1995–2007 (1999).
[52]A. Clarke and E. Stattersfield, "Direct evidence supporting nonlocal hydrodynamic influence on the dynamic contact angle," Phys. Fluids **18**, 048106 (2006).
[53]J. E. Sprittles and Y. D. Shikhmurzaev, "Finite element simulation of dynamic wetting flows as an interface formation process," J. Comput. Phys. **233**, 34–65 (2013).
[54]J. E. Sprittles and Y. D. Shikhmurzaev, "Corrigendum to 'Finite element simulation of dynamic wetting flows as an interface formation process' [J. Comput. Phys. 233 (2013) 34–65]," J. Comput. Phys. **274**, 936 (2014).
[55]L. A. Dorfman, "Flow and heat transfer in a viscous liquid layer on a spinning disc," J. Eng. Phys. **12**, 162 (1967).
[56]J. W. Rauscher, R. E. Kelly, and J. D. Cole, "An asymptotic solution for the laminar flow of thin films on a rotating disk," J. Appl. Mech. **40**, 43–47 (1973).
[57]G. M. Sisoev, A. F. Tal'drik, and V. Y. Shkadov, "Flow of a viscous liquid film on the surface of a rotating disc," J. Eng. Phys. **51**, 1171–1174 (1986).
[58]G. M. Sisoev and V. Y. Shkadov, "Flow stability of a film of viscous liquid on the surface of a rotating disc," J. Eng. Phys. **52**, 671–674 (1987).
[59]G. M. Sisoev and V. Y. Shkadov, "Helical waves in a liquid film on a rotating disc," J. Eng. Phys. **58**, 423 (1990).
[60]G. M. Sisoev, O. K. Matar, and C. J. Lawrence, "Stabilizing effect of the Coriolis forces on a viscous liquid film flowing over a spinning disc," C. R. Mec. **332**, 203–207 (2004).
[61]O. K. Matar, C. J. Lawrence, and G. M. Sisoev, "The flow of thin liquid films over spinning discs: Hydrodynamics and mass transfer," Phys. Fluids **17**, 052102 (2005).
[62]V. Y. Shkadov, "Wave flow regimes of a thin layer of viscous fluid subject to gravity," Fluid Dyn. **2**, 29–34 (1967).
[63]V. Y. Shkadov and G. M. Sisoev, "Waves induced by instability in falling films of finite thickness," Fluid Dyn. Res. **35**, 357–389 (2004).
[64]O. K. Matar, G. M. Sisoev, and C. J. Lawrence, "Evolution scales for wave regimes in liquid film flow over a spinning disk," Phys. Fluids **16**, 1532–1545 (2004).
[65]V. Y. Shkadov and G. M. Sisoev, "Wavy falling liquid films: Theory and computation instead of physical experiment," in IUTAM Symposium on Nonlinear Waves in Multi-Phase Flow, Fluid Mechanics and Its Applications Vol. 57, edited by H.-C. Chang (Kluwer, Notre Dame, USA, 2000), pp. 1–10.
[66]G. M. Sisoev and V. Y. Shkadov, "A two-parameter manifold of wave solutions to an equation for a falling film of a viscous fluid," Dokl. Phys. **44**, 454–459 (1999).
[67]L. Ting and J. B. Keller, "Slender jets and thin sheets with surface tension," SIAM J. Appl. Math. **50**, 1533–1546 (1990).
[68]P. M. Gresho and R. L. Sani, *Incompressible Flow and the Finite Element Method, Volume 1: Advection-Diffusion* (John Wiley & Sons, NY, 1999).
[69]J. E. Sprittles and Y. D. Shikhmurzaev, "Finite element framework for describing dynamic wetting phenomena," Int. J. Numer. Methods Fluids **68**, 1257–1298 (2012).
[70]R. A. Cairncross, P. R. Schunk, T. A. Baer, R. R. Rao, and P. A. Sackinger, "A finite element method for free surface flows of incompressible fluids in three dimensions. Part I. Boundary fitted mesh motion," Int. J. Numer. Methods Fluids **33**, 375–403 (2000).
[71]S. F. Kistler and L. E. Scriven, "Coating flow theory by finite element and asymptotic analysis of the Navier-Stokes system," Int. J. Numer. Methods Fluids **4**, 207 (1984).
[72]A. K. Aziz, *Mathematical Foundations of the Finite Element Method with Applications to Partial Differential Equations* (Academic Press, New York, 1972).
[73]D. Wang, X. Ling, and H. Peng, "Simulation of ligament mode breakup of molten slag by spinning disk in the dry granulation process," Appl. Therm. Eng. **84**, 437–447 (2015).
[74]D. Wang, X. Ling, and H. Peng, "Theoretical analysis of free-surface film flow on the rotary granulating disk in waste heat recovery process of molten slag," Appl. Therm. Eng. **63**, 387–395 (2014).
[75]H. Ouyang, "Vibration of an atomising disc subjected to a growing distributed mass," J. Mech. Phys. Solids **53**, 1000–1014 (2005).
[76]Y. Y. Zhao, "Consideration in designing a centrifugal atomiser for metal powder production," Mater. Des. **27**, 745–750 (2006).
[77]H. B. Eral, D. J. C. M. Mannetje, and J. M. Oh, "Contact angle hysteresis: Review of fundamentals and applications," Colloid Polym. Sci. **291**, 247–260 (2013).
[78]X. Yang and A. Turan, "Simulation of liquid jet atomization coupled with forced perturbation," Phys. Fluids **29**, 022103 (2017).
[79]P. Eisenklam, "On ligament formation from spinning discs and cups," Chem. Eng. Sci. **19**, 693–694 (1964).
[80]T. Kamiya, "An analysis of the ligament-type disintegration of thin liquid film at the edge of a rotating disk," J. Chem. Eng. Jpn. **5**, 391–396 (1972).